

Towards high-throughput many-body perturbation theory: efficient algorithms and automated workflows

Miki Bonacci,^{1,2,*} Junfeng Qiao,³ Nicola Spallanzani,² Antimo Marrazzo,⁴ Giovanni Pizzi,^{3,5} Elisa Molinari,^{1,2} Daniele Varsano,² Andrea Ferretti,² and Deborah Prezzi²

¹*FIM Department, University of Modena and Reggio Emilia, Via Campi 213/a, Modena, Italy*

²*S3 Center, Istituto Nanoscienze, CNR, Via Campi 213/a, Modena, Italy*

³*Theory and Simulation of Materials (THEOS) and National Centre for Computational Design and Discovery of Novel Materials (MARVEL),*

École Polytechnique Fédérale de Lausanne, CH-1015 Lausanne, Switzerland

⁴*Dipartimento di Fisica, Università di Trieste, I-34151 Trieste, Italy*

⁵*Laboratory for Materials Simulations (LMS), Paul Scherrer Institut (PSI), CH-5232 Villigen PSI, Switzerland*

(Dated: January 19, 2023)

The automation of ab initio simulations is essential in view of performing high-throughput (HT) computational screenings oriented to the discovery of novel materials with desired physical properties. In this work, we propose algorithms and implementations that are relevant to extend this approach beyond density functional theory (DFT), in order to automate many-body perturbation theory (MBPT) calculations. Notably, a novel algorithm pursuing the goal of an efficient and robust convergence procedure for GW and BSE simulations is provided, together with its implementation in a fully automated framework. This is accompanied by an automatic GW band interpolation scheme based on maximally-localized Wannier functions, aiming at a reduction of the computational burden of quasiparticle band structures while preserving high accuracy. The proposed developments are validated on a set of representative semiconductor and metallic systems.

I. INTRODUCTION

Computational HT screening is nowadays a consolidated approach to materials discovery,^{1–3} as a complementary and accelerated tool with respect to experimental efforts. In the last decade, seminal works in this field have addressed, among many other topics, the discovery of novel 2D materials,^{4–10} the identification of optimal new lithium-ion battery anodes,^{11,12} thermoelectric,^{13,14} photocatalysts¹⁵ and photovoltaic light harvesting^{16–18} materials. The success of these studies relies on the development of different software and implementations¹⁹ that were able to encode complex domain-specific knowledge into automated and robust workflows – enforcing rigorous computational protocols^{19,20} and managing all the steps concerning a simulation – which thus require the least possible human intervention.^{21–29}

Concerning the electronic structure field, most of these works and implementations are based on DFT, which allows one to compute total energies, optimized geometries, and other ground state properties of materials with predictive accuracy. However, different approaches are required for the accurate prediction of excited-state properties of materials, such as quasiparticle (QP) band structures and absorption spectra, which are typically crucial for the description of active processes in modern optoelectronic technologies, like photovoltaics, photocatalysis, light-emitting diodes (LEDs), photodetectors and solar cells.^{30–36} In this context, MBPT and Green’s function methods represent the state-of-the-art tools, where charged (electronic quasi-particle levels) and neutral excitations (optical properties, electron energy loss spectra) can be obtained by means of the GW approximation and

the Bethe-Salpeter equation (BSE), respectively.³⁷

To date, a limited number of attempts have been made toward automation³⁸ and HT screening^{9,39} based on these MBPT approaches, mainly because of their conceptual and computational complexity. Indeed, depending on the specific physical problem, different levels of theory might be adopted,⁴⁰ further branching off depending on the chosen approximations and implementations.^{41,42} Furthermore, even for the simplest approximations, these calculations require the control over a much larger parameter space with respect to DFT, with parameters that are often interdependent and might change depending on the specific implementations adopted, but the choice of which is always crucial to obtain reliable results. From a computational point of view, this type of simulations are constituted by a chain of distinct steps, often relying on the usage of different software tools, each of them with their own specificity, e.g., in terms of memory and parallelization requirements. Memory requirements are much heavier than in standard DFT simulations even for moderate system size, and often require massive usage of parallel computing resources. Calculations often fail due to memory overflow and have to be restarted with careful choice of parameters. All of these problems make the application of MBPT-based approaches a complex and difficult task per se, and its automation still an open challenge.

Building on pioneering works in the field,^{38,39} we here focus on the development of an improved algorithm aiming at an efficient and computationally cost-effective management of the choice of converged parameters for accurate GW-BSE calculations. The algorithm is implemented in the AiiDA framework,^{28,29} a platform that is routinely used for HT studies^{6,43–45} and that incorpo-

rates the ADES model for Automation, Data, Environment and Sharing.²⁴ As detailed below, this implementation allows us to encode an efficient error handling, memory and parallelization management, and logic computational flows within automated python workflows. Moreover, it guarantees a seamless interoperability of different software codes that tackle the different steps usually involved in MBPT simulations, i.e., the preliminary DFT part (here using QUANTUM ESPRESSO^{46,47}), the GW-BSE calculations (YAMBO^{48,49}), and any required post-processing. In particular, for the latter, we here introduce a scheme based on maximally localized Wannier functions⁵⁰ for the automatic interpolation of GW band structures, which interfaces the WANNIER90⁵¹ and YAMBO projects. All of these developments point to a drastic reduction of both human and computational efforts, key issues for enabling HT studies. In addition, by incorporating the different domain-specific scientific and computational competences into robust and reliable workflows, we aim at making accurate GW-BSE calculations available for the materials science community at large, including non-experts in the field (e.g., via graphical user interfaces⁵²), similarly to what has already happened with DFT.

The manuscript is organised as follows. In the Results and Discussion Section, we first introduce a model for the convergence surface in the N-dimensional space of the GW (BSE) variables, and present our improved algorithm for efficiently retrieving converged values for the main (interdependent) parameters. The implementation of this algorithm within the `aiida-yambo` plugin is then described, followed by the presentation of the novel `aiida-yambo-wannier90` plugin that encodes the GW band interpolation based on Wannierization. Both these implementations are validated for selected prototypical systems. Additional details on simulations are provided in the Methods section. In the remainder of this section, we instead introduce the main concepts and quantities related to the GW and BSE schemes, which will be useful to properly understand the subsequent Sections.

GW approximation

Accurate electronic band structures of materials can be computed within the MBPT framework by correcting the Kohn-Sham (KS) DFT eigenvalues with a self-energy term Σ by means of the *GW* approximation, i.e.

Σ is approximated with the first term of the perturbation series expansion in terms of the screened Coulomb interaction W .⁵³ We hereafter consider the simplest and most widespread implementation of GW, i.e. the so-called G_0W_0 approach, where G_0 is the KS independent-particle one-body Green's function and W is computed within the random-phase approximation (RPA).⁵⁴ Nevertheless, the convergence algorithm presented here can be used also for more sophisticated flavours of the theory, e.g. the self-consistent GW. Under these assumptions and by considering a plane-wave expansion, the self-energy term $\Sigma_{n\mathbf{k}}$ for a band n at a given \mathbf{k} -point – written as the sum of the Fock exchange (Σ^x) and the frequency-dependent correlation (Σ^c) terms – is given by:

$$\Sigma_{n\mathbf{k}}^x = - \sum_m^{\text{occ}} \int \frac{d\mathbf{q}}{(2\pi)^3} \sum_{\mathbf{G}}^{G_{\text{cut}}^x} v_{\mathbf{G}}(\mathbf{q}) |\rho_{nm}(\mathbf{k}, \mathbf{q}, \mathbf{G})|^2 f_{m, \mathbf{k}-\mathbf{q}} \quad (1)$$

and

$$\Sigma_{n\mathbf{k}}^c(\omega) = -i \sum_m^{N_b} \int \frac{d\mathbf{q}}{(2\pi)^3} \sum_{\mathbf{G}\mathbf{G}'}^{G_{\text{cut}}} \rho_{nm}(\mathbf{k}, \mathbf{q}, \mathbf{G}) \rho_{nm}^*(\mathbf{k}, \mathbf{q}, \mathbf{G}') \times \int d\omega' W_{\mathbf{G}\mathbf{G}'}(\mathbf{q}, \omega') \times \left[\frac{f_{m, \mathbf{k}-\mathbf{q}}}{\omega - \omega' - \epsilon_{m, \mathbf{k}-\mathbf{q}} - i\eta} + \frac{1 - f_{m, \mathbf{k}-\mathbf{q}}}{\omega - \omega' - \epsilon_{m, \mathbf{k}-\mathbf{q}} + i\eta} \right], \quad (2)$$

where $v_{\mathbf{G}}(\mathbf{q})$ and $W_{\mathbf{G}\mathbf{G}'}(\mathbf{q}, \omega')$ are the bare and screened Coulomb interaction, respectively. The generalized dipole matrix elements $\rho_{nm}(\mathbf{k}, \mathbf{q}, \mathbf{G})$ are defined as:

$$\rho_{nm}(\mathbf{k}, \mathbf{q}, \mathbf{G}) = \langle n\mathbf{k} | e^{i(\mathbf{q}+\mathbf{G})\cdot\mathbf{r}} | m\mathbf{k} - \mathbf{q} \rangle, \quad (3)$$

where $\epsilon_{n\mathbf{k}}^{\text{KS}}$ and $|n\mathbf{k}\rangle$ are the corresponding KS eigenvalues and eigenvectors. Here, W can be written in terms of the reducible polarizability χ ($W = v + v\chi v$), which is in turn computed by solving a Dyson equation for the RPA irreducible polarizability χ^0 :

$$\chi_{\mathbf{G}\mathbf{G}'}(\mathbf{q}, \omega) = \sum_{\mathbf{G}''}^{G_{\text{cut}}} [I - v(\mathbf{q})\chi^0(\mathbf{q}, \omega)]_{\mathbf{G}\mathbf{G}''}^{-1} \chi_{\mathbf{G}''\mathbf{G}'}^0(\mathbf{q}, \omega), \quad (4)$$

where

$$\chi_{\mathbf{G}\mathbf{G}'}^0(\mathbf{q}, \omega) = 2 \sum_{nm}^{N_b} \int_{BZ} \frac{d\mathbf{k}}{(2\pi)^3} \rho_{mn}^*(\mathbf{k}, \mathbf{q}, \mathbf{G}) \rho_{mn}(\mathbf{k}, \mathbf{q}, \mathbf{G}') \left[\frac{f_{n\mathbf{k}-\mathbf{q}}(1 - f_{m\mathbf{k}})}{\omega + \epsilon_{n\mathbf{k}-\mathbf{q}} - \epsilon_{m\mathbf{k}}} - \frac{f_{n\mathbf{k}-\mathbf{q}}(1 - f_{m\mathbf{k}})}{\omega + \epsilon_{m\mathbf{k}} - \epsilon_{n\mathbf{k}-\mathbf{q}}} \right]. \quad (5)$$

In practice, the above quantities are computed by in-

roducing specific approximations that crucially impact

both the accuracy and the computational and memory costs of the calculations. In particular, Eq. (4) as well as Eq. (2) involve a discrete, finite number of \mathbf{G} vectors, set by a cutoff parameter G_{cut} , which defines the size of the response matrix. Moreover, with the parameter N_b , we introduce a truncation over the KS states summation for both response $\chi_{\mathbf{G}\mathbf{G}'}^0$ (Eq. (5)) and self-energy Σ^c (Eq. (2)), which should in principle include all occupied and an infinite number of empty states. Finally, all the integrals in reciprocal space are computed on a discrete \mathbf{k} -points (\mathbf{q} -points) grid whose size, $N_{\mathbf{k}}$, defines the accuracy of the sampling of the Brillouin zone (BZ). All of these three parameters, G_{cut} , N_b , and $N_{\mathbf{k}}$, need to be increased till the desired convergence is reached.

One of the major obstacles to automate the convergence procedure lies in the interdependence of the first two parameters, G_{cut} and N_b , such that their convergence has to be performed *jointly*, as thoroughly discussed elsewhere.^{38,42,55} Indeed, Eqs. (4) and (5) contains a summation over both empty states and reciprocal lattice vectors (\mathbf{G}), and the expression of the generalized dipole terms in Eq. (3) is such that matrix elements with large \mathbf{G} are governed by high-energy KS states.³⁸ Furthermore, the interdependence is non-trivial, given the presence of an inversion in Eq. (4) that further enters in the evaluation of the correlation self-energy, Eq. (2). Given the lack of an efficient “recipe” to carry out this non-trivial, coupled convergence, one has to resort to an iterative convergence of each of the two parameters by fixing the other, in an alternating way. This procedure, in addition of being tedious, is computationally very expensive, sometimes representing the most cumbersome part of a GW calculation.

Bethe-Salpeter Equation

Starting from the GW quasi-particles, the solution of the BSE^{54,56} can give access to optical properties of materials via the macroscopic dielectric function:

$$\epsilon_M(\omega, \mathbf{q}) = 1 - \frac{2}{VN_q} v(\mathbf{q}) \sum_{\lambda} \Phi_{\lambda}(\mathbf{q}) \times \left[\frac{1}{E^{\lambda}(\mathbf{q}) - (\omega + i\eta)} + \frac{1}{E^{\lambda}(\mathbf{q}) + (\omega + i\eta)} \right], \quad (6)$$

where V is the volume of the unit cell; N_q is the number of \mathbf{q} -points sampling the Brillouin zone (BZ); $E^{\lambda}(\mathbf{q})$ is the eigenvalue of the exciton λ at momentum $\mathbf{q} = \mathbf{k} - \mathbf{k}'$, and the corresponding exciton oscillator strength $\Phi_{\lambda}(\mathbf{q})$ is defined as:

$$\Phi_{\lambda}(\mathbf{q}) = \left| \sum_{(vc,\mathbf{k})} \langle v\mathbf{k} - \mathbf{q} | e^{-i\mathbf{q}\cdot\mathbf{r}} | c\mathbf{k} \rangle A_{vc\mathbf{k}}^{\lambda}(\mathbf{q}) \right|^2. \quad (7)$$

Equation (7) contains a summation over valence and conduction bands (v, c), and \mathbf{k} -point mesh, which are

the main parameters to converge for a BSE calculation. The terms $A_{vc\mathbf{k}}^{\lambda}(\mathbf{q})$ represent the weight of each electron-hole transition contributing the exciton λ , as resulting from the solution of the BSE. The summation over bands mainly defines the range of energies under investigation. The \mathbf{k} -point mesh is connected to the accuracy with which we describe the exciton composition in terms of single-particle $v \rightarrow c$ transitions over the entire BZ, and it is usually significantly larger than the one needed to converge the corresponding GW band structure. Additional convergence parameters are the number of \mathbf{G} vectors used for expanding the KS wave-functions in the transition matrix elements, as defined in Eq. (3), and for Fast-Fourier-Transform (FFT) operations, as well as the plane-wave expansion of the BSE kernel (both direct and exchange terms). These parameters are usually inherited from GW convergences.

II. RESULTS AND DISCUSSION

Description of the convergence surface

The above-described coupled convergence of the parameters, combined with a much worse scaling than DFT and more computationally and memory demanding calculations, call for efficient procedures to describe and explore the convergence space in GW-BSE simulations. A possible strategy is to describe the convergence space in terms of an analytic function of the parameters.^{38,39,41,57–59} For a general $(N+1)$ dimensional space, a model convergence surface $f(\mathbf{x})$ that represents the value of a given observable $E(\mathbf{x})$ (e.g., quasiparticle energies or excitonic eigenvalues) as a function of the N parameters $\mathbf{x} = [x_1, \dots, x_N]$ can be defined as:

$$f(\mathbf{x}) = \prod_i^N \left(\frac{A_i}{x_i^{\alpha_i}} + b_i \right), \quad (8)$$

where A_i , b_i and α_i are free fitting parameters, and $B = \prod_i^N b_i$ is the extrapolated converged value. Of course, the accuracy of the latter depends on the actual region of the parameter space explored for the evaluation of the convergence behaviour, i.e., how far is the extrapolated value from the exact one. As such, B might not always be a good choice for guiding the search of the convergence parameters.

In the following, we introduce conditions on the mixed partial derivatives of Eq. (8) as a way to address the parameter interdependence. Indeed, the adoption of an analytical form for the description of the convergence space has the clear advantage of enabling the calculation of all-order derivatives, once the fitting parameters are known. On the other hand, not taking directly into account this interdependence can result in a very tedious convergence procedure, as it would require the cyclic repetition of multiple univariate convergences, as mentioned in the In-

roduction (further details are provided in Supplemental Material⁶⁰ and Ref. 49).

For the expression in Eq. (8), the gradient components are:

$$f'_{x_i}(\mathbf{x}) = -\alpha_i \frac{A_i}{x_i^{\alpha_i+1}} \prod_{j \neq i}^N \left(\frac{A_j}{x_j^{\alpha_j}} + b_j \right), \quad (9)$$

while second derivatives are:

$$f''_{x_i}(\mathbf{x}) = \alpha_i(\alpha_i + 1) \frac{A_i}{x_i^{\alpha_i+2}} \prod_{j \neq i}^N \left(\frac{A_j}{x_j^{\alpha_j}} + b_j \right), \quad (10)$$

$$f''_{x_i, x_j}(\mathbf{x}) = \alpha_i \alpha_j \frac{A_i A_j}{x_i^{\alpha_i+1} x_j^{\alpha_j+1}} \prod_{k \neq i, j}^N \left(\frac{A_k}{x_k^{\alpha_k}} + b_k \right). \quad (11)$$

The asymptotic region of the convergence surface can be determined by imposing, for each parameter x_i, x_j with $i, j = 1, \dots, N$, two conditions:

$$\begin{cases} |f'_{x_i}(\mathbf{x})| < \Delta_i \\ |f''_{x_i, x_j}(\mathbf{x})| < \Delta_{ij} \end{cases} \quad (12)$$

The first condition determines the region in which the convergence surface becomes flat (thus approaching convergence), whereas the condition on second partial derivatives ensures that the N parameters are no longer interdependent. The threshold values Δ_i and Δ_{ij} can be tuned according to the desired accuracy.⁷⁹ Once this asymptotic region has been determined, a guess for the converged value of $f(\mathbf{x})$, E_{guess} , is made, and its accuracy is then checked and validated according to the automated algorithm described below.

Convergence algorithm

Figure 1 schematically depicts our convergence algorithm, which is purposed to obtain the desired accuracy on GW-BSE results with the least possible number of calculations. In the following, we consider N_b and G_{cut} as the two interdependent parameters to be converged simultaneously. We remark that, while the algorithm is specifically designed to handle coupled convergences, it can be successfully used to accelerate convergence tests with respect to any other parameter, such as the BZ \mathbf{k} -point mesh or the FFT grids.

The first step (i) consists in the construction of the N -dimensional space of parameters as a grid of equally spaced points, with spacing and ranges provided from input. It is worth noting that, to fit the functional form of Eq. (8), one needs to generate a grid with minimum $3N$ points, since $f(\mathbf{x})$ contains three free fitting parameters for each of the N dimensions of the parameter space. However, a further reduction on the minimal grid size

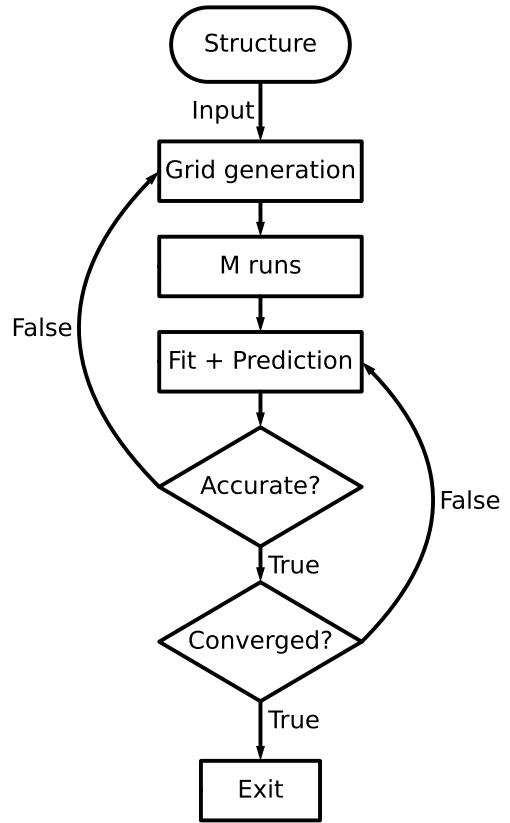


FIG. 1: **Flowchart of the convergence algorithm.** After generating the grid for the N -dimensional parameter space, a subset of M simulations is performed. The results are then fitted to predict the converged parameters. Finally, the accuracy (Eq. (13)a) and the convergence (Eq. (13)b) of the prediction are verified, and the procedure iterated, if needed.

(that is, on the minimum number of calculations to perform) can be obtained by fixing the power-law dependence, α_i , to a given value, as suggested in Ref. 38, thus resulting in a minimal grid size of $2N$. Usually, much denser grids are generated, where (ii) $M_0 \geq 2N$ calculations are performed on a subset of the grid points, chosen such as to efficiently sample the parameter space.

Next (iii), the results of the calculations are fitted by using the expression Eq. (8). As mentioned above, the power laws are fixed to given values: $\alpha_i \in \{1, 2\} \forall i=1, \dots, N$, and the one resulting in the lowest mean squared error is chosen. The asymptotic region is then identified by computing the first and second order derivatives (Eqs. (9)-(11)), and imposing the conditions in Eq. (12). Given the asymptotic region, a guess converged value is selected $E_{guess} = f(N_b^0, G_{cut}^0)$, where (N_b^0, G_{cut}^0) are the lowest values that can be chosen for the parameters such that E_{guess} is within a desired convergence threshold Δ with respect to the asymptotic region.

To establish the accuracy and convergence of the fitting procedure, (iv) $E(N_b^0, G_{cut}^0)$ is computed and compared to the outcome of the fit E_{guess} , by considering the cho-

sen threshold Δ (see Eq. (13)a below). If the accuracy condition is satisfied, we need to check the convergence of the fitting procedure, that is, a new pair of parameters (N_b^1, G_{cut}^1) is obtained from the fit by adding the (N_b^0, G_{cut}^0) point to the initial M_0 grid, and compared to the previous one (see Eq. (13)b below). The last step is repeated until convergence is reached. If the accuracy condition is not satisfied, the grid is instead shifted toward higher values of the parameters, and the steps (ii)-(iv) are repeated until the two conditions:

$$|E(N_b^j, G_{cut}^j) - E^{fit}(N_b^j, G_{cut}^j)| < \Delta \quad (13a)$$

$$(N_b^{j+1}, G_{cut}^{j+1}) = (N_b^j, G_{cut}^j), \quad (13b)$$

are simultaneously satisfied for the j -th iteration.

The aiiida-yambo plugin and automated workflows

The above convergence algorithm has been implemented in the new version of the `aiida-yambo` plugin,⁶¹ which is meant to fully automate GW-BSE calculations by interfacing the YAMBO project^{48,49} and the AiiDA informatics infrastructure and workflow management system.^{28,29} The automation concerns input generation, scheduler submission, and output parsing phases.⁸⁰ Thanks to the AiiDA infrastructure, links between single calculations are managed on the fly by ad-hoc, *dynamic* workflows (the so-called *workchains* in the AiiDA jargon), i.e. their execution path is not fixed, but can depend on the results of completed calculations. This allows for the implementation of complex logics, such as those characterizing the convergence algorithm and GW band interpolation that we propose in this work. Moreover, each calculation, together with inputs and outputs, is stored in the AiiDA relational database, thus ensuring data provenance and full reproducibility of results.

Currently, the `aiida-yambo` plugin supports quasiparticle (G_0W_0 and COSHEX⁵³ level) and optical properties (IP-RPA and BSE) simulations, as well as interfaces with different codes (e.g., QUANTUM ESPRESSO and WANNIER90). These options are implemented in the `YamboCalculation` and `YppCalculation` classes, which manage individual simulations (including data interfacing) that can be performed by using the YAMBO code. On top of them, task-specific workflows are implemented, and organized in a modular way, in order to automate tasks of increasing complexity. In particular, the `aiida-yambo` plugin contains three main workflows, each of them targeting a precise task:

- **YamboRestart**: automation of error handling and restart for each `YamboCalculation`;
- **YamboWorkflow**: automation of the single GW or BSE flow (composed of several interlinked steps, explained in the following);

- **YamboConvergence**: automation of the convergence (composed of multiple `YamboWorkflow` runs).

Their nested organization is shown in Fig. 2.

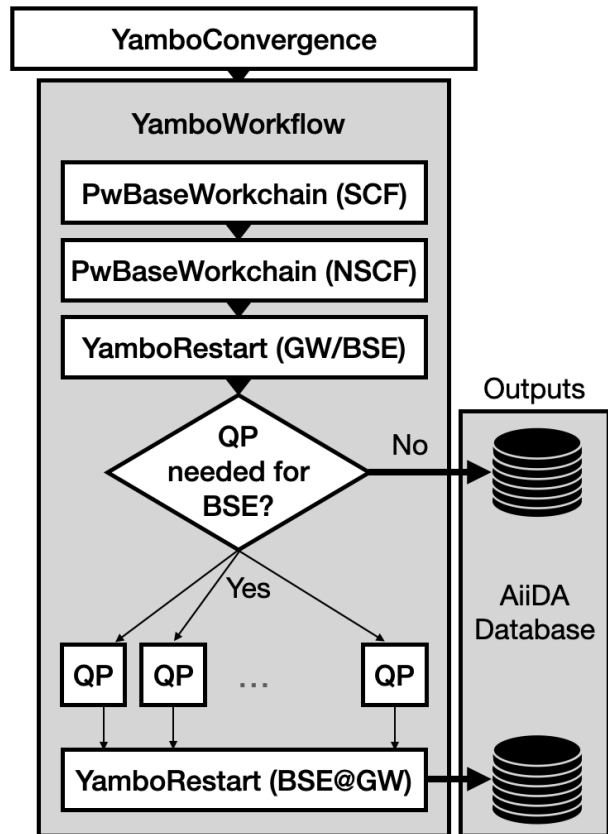


FIG. 2: **Hierarchical structure of the aiiida-yambo workchains.** The highest level workflow is `YamboConvergence`, which calls multiple `YamboWorkflow` workchains. `YamboWorkflow` comprises all the steps needed to perform individual GW-BSE calculations from scratch. In case of failures, it calls the `YamboRestart` workchain for automatic error handling. The outputs are stored in the AiiDA database in a human readable fashion, and are easily accessible and shareable by the user.

The highest level workflow is represented by the `YamboConvergence` workchain, which implements the full automation of the convergence algorithm of Sec. II, thus allowing for all YAMBO simulations to be organized on the fly, without any external user intervention. The user is only requested to provide a python list containing the information on the parameter space to be explored. An example of such input reads:

```
[
  {
    'var': [
      'BndsRnXp',
      'GbnDRnge',
      'NGsBlkXp'
    ]
  }
]
```



```

'start ': [50, 50, 2],
'stop ': [400, 400, 10],
'delta ': [50, 50, 2],
'max ': [1000, 1000, 36],
'what ': ['gap_GG'],
'conv_thr ': 0.1,
'conv_thr_units ': 'eV',
},
]

```

where the YAMBO variables “BndsRnXp” and “Gbn-dRnge” govern the convergence over empty states, N_b , to be carried out jointly with that on the size of the response matrix, G_{cut} (“NGsBlkXp” variable). The edges of the grid (“start” and “stop”) and its spacing (“delta”), together with an upper bound of the parameter space (“max”), limiting the search to computationally accessible calculations, are also set by the user. The key “what” indicates the quantity to be converged – in our example, the direct band gap of the material at Γ point – up to a given convergence threshold Δ (“conv_thr” key). The output summarizes the convergence history and allows the user to easily parse the converged simulation. `YamboConvergence` allows one to converge several many-body quantities, like quasiparticle levels, band-gaps, as well as optical excitation energies. Notably, the convergence block in Fig. 2 can be skipped if converged parameters are already known.

Each single GW (BSE) calculation is instead automated within `YamboWorkflow`, which is the core workflow of the plugin that takes care of performing all the steps needed in a typical YAMBO simulation – from preliminary self-consistent (SCF) and non-self-consistent (NSCF) DFT calculations to the actual GW (BSE) calculations, and the related post-processing. The workflow ensures a robust interoperability between DFT and MBPT codes (QUANTUM ESPRESSO and YAMBO, respectively), and links subsequent calculations, interfacing the data automatically. In practice, `YamboWorkflow` encodes the specific flowchart underlying each requested calculation, and allows for its dynamic execution according to the instructions provided in input. This implies performing all the intermediate steps needed for a specific calculations without the need of instructing them explicitly, or, on the contrary, to skip some of the intermediate steps for which parent calculations are available, fully exploiting the `YamboWorkflow` provenance information.

To support a restart mechanism in case of code failures, `YamboWorkflow` takes advantage of the `YamboRestart` workflow, a sub-level workflow that encodes an automatic error handler (inherited from the `AiiDA BaseRestartWorkchain` class) which, depending on the encountered failure, automatically instructs a restart run. For out-of-memory errors or failures connected with insufficient wall-time requests, `YamboRestart` automatically resubmits the calculation by appropriately changing the requested resources (e.g., the maximum wall-time and the MPI/OpenMP balance); parallelization errors

are managed by overwriting the parallelism variables set in input by the user with the default parallelism decided on the fly by `yambo`. In all these cases, an efficient, CPU-time saving restart mechanism is implemented, which avoids to restart unfinished runs from scratch by automatically retrieving and enabling the reuse of stored data files.

As a final issue, we would like to discuss the possibility to develop protocols for MBPT calculations. Indeed, most of the DFT-based AiiDA plugins enable the use of protocols,⁶² that is, the possibility of creating inputs with pre-populated default values for several parameters. Such protocols are usually code-agnostic and robust, given the high level of reproducibility of DFT with different quantum engines.¹⁹ Moreover, their reliability is guaranteed by means of large scale studies spanning systems with a wide variety of characteristics (i.e., metals, semiconductors, dimensionality and so on).⁴⁴

Concerning MBPT calculations, the possibility to define protocols is still an open issue.³⁸ First of all, code-agnostic parameters are not at all easy to be determined as it is for DFT-based codes, because the MBPT implementations and the subsequent definition of parameters can differ in very many aspects, as highlighted in the Introduction section. Secondly, the high computational cost of these simulations has limited so far the number of systems to be studied extensively, which is crucial to define a reliable statistics on convergence parameters. Last but not least, DFT-based protocols usually result in safe but overconverged parameters, an approach that might lead to unfeasible calculations when moving to the GW-BSE framework.

For all these reasons, we believe that an efficient, fully automated convergence tool, as the one presented here, is currently the most valuable solution. Nonetheless, also in view of possible future developments, the `aaiida-yambo` plugin provides an implementation for a protocol framework for both GW and BSE simulations, which is currently pre-populated on the basis of previous experience on a limited subset of systems. Such protocols concern several parameters connected to the main `yambo` input variables, such as the FFT grids (“FFTGvecs”), the summation over empty states (“BndsRnXp” and “Gbn-dRnge”), the plane-wave expansion for the polarizability (“NGsBlkXp”) and the BZ k -point sampling. A detailed documentation on these and other aspects concerning the `aaiida-yambo` plugin is provided elsewhere.⁶³

Automatic GW bands interpolation: the `aaiida-yambo-wannier90` plugin

GW band interpolation from Wannierization is a crucial task in order to obtain the most accurate quasiparticle band structure with the lowest computational cost. This task is encoded in the `aaiida-yambo-wannier90` plugin.^{64,65} Essentially, the plugin provides a meta-workflow, called `YamboWannier90WorkChain`, which uti-

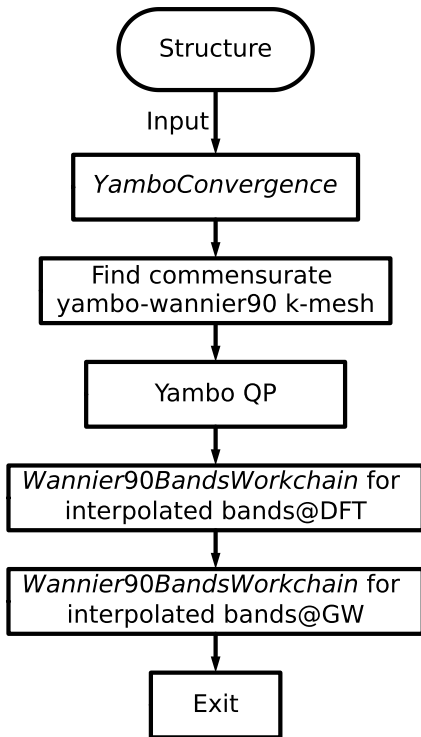


FIG. 3: **Flowchart of the YamboWannier90WorkChain** for the Wannier interpolation of GW band structures. After performing the `YamboConvergence`, the workflow searches for a commensurate k-point meshes for `Yambo` and `Wannier90`, and carries out the corresponding `Yambo QP` calculation. Given the QP corrections, the workflow proceeds with the Wannierization and the band interpolation at DFT and GW level.

lizes the automation and error handling of the underlying `aiida-yambo` and `aiida-wannier90-workflows` plugins for GW convergence and Wannierization, respectively. The flowchart of the workflow is summarized in Fig. 3. Starting from a given crystal structure, the workflow first launches a `YamboConvergence` workflow for automatic convergence. Then, it finds the minimal commensurate mesh with the `Wannier90` ones that satisfies the GW convergence conditions (see below). Thirdly, it runs `YamboWorkflow` to compute all the quasiparticle corrections required for the Wannierization on the commensurate mesh, and a subsequent `ypp` calculation (by means of `YppRestart`) to extract the GW corrections in a `Wannier90 eig` file format. Fourthly, the workflow Wannierizes the KS wavefunctions, saving the unitary transformation matrices of maximal localization, and interpolates the band structure. Finally, the workflow performs the Wannierization procedure at G_0W_0 level, which consists in incorporating the GW corrections into the DFT eigenvalues, and interpolating the band structure by using the DFT Wannierization outcomes.

A crucial step of the workflow is finding a commensurate mesh for both GW QP calculations and Wan-

nierization. Indeed, the GW mesh resulting from automated convergence might not always be compatible with the mesh required by `Wannier90` to ensure interpolation accuracy. Notably, considering a Monkhorst-Pack (MP) grid for the Wannierization, the corresponding GW mesh must be an integer multiple of the MP grid. We here propose a recipe to find the minimal commensurate meshes for GW and `Wannier90` calculations, as depicted in Fig. 4. Considering n_d as the number of k-points chosen by the `YamboConvergence` workflow, and n_c the number of k-points chosen by the Wannierization protocol (typically based on a k-point spacing, 0.2 \AA^{-1})⁴⁵, the target is to find a new (n'_d, n'_c) such that the dense mesh $n'_d = k \cdot n'_c$, where $k \in \mathbb{N}$, i.e., natural number. The given input (n_d, n_c) restricts the search space to a sector bounded by k_{low} and k_{high} (see Fig. 4), where $k_{\text{low}} = 1$ ($n'_d = n'_c = \max(n_d, n_c)$ is always a good solution), and $k_{\text{high}} = \lceil \frac{n_d}{n_c} \rceil$, where $\lceil \cdot \rceil$ indicates the ceiling integer. The search always succeeds since $s_{\text{low}} = (\max(n_d, n_c), \max(n_d, n_c))$ and $s_{\text{high}} = (k_{\text{high}} \cdot n_c, n_c)$ are already two good solutions. In fact, the optimal solution is often inside the triangular region determined by the input (n_d, n_c) , s_{low} , and s_{high} . The final solution is chosen according to the ℓ^1 distance to the input, such to ensure the minimal increase in computational cost. It is also possible to change the metric, e.g., pushing the solution towards increasing the Wannier mesh or GW mesh, depending on which calculation is less cumbersome. The aforementioned recipe is repeated for each of the three dimensions of the MP grid.

Validation of the workflows

The proposed convergence algorithm, as implemented in the `YamboConvergence` workflow, has been validated by performing convergence studies for the quasiparticle G_0W_0 gap of a set of prototypical semiconductors: silicon, diamond, ZnO, rutile TiO_2 , monolayer MoS_2 , bulk and monolayer hBN. The convergence addresses the direct band gap at the Γ point with respect to the two coupled parameters, N_b and G_{cut} , and the \mathbf{k} -point grid (in terms of \mathbf{k} -points density $\rho_{\mathbf{k}}$). Once convergence is achieved, the minimum band gap $E_{\text{gap}}^{G_0W_0}$ is also computed. The results are summarized in Table I, where, together with $E_{\text{gap}}^{G_0W_0}$, we report the final parameters resulting from the convergence procedure (N_b , G_{cut} , and $\rho_{\mathbf{k}}$) as well as the convergence threshold (absolute, $\Delta_{\%}^{\Gamma}$, and relative, $\Delta_{\%}^{\Gamma}$) adopted in each case. Our results are found in good agreement with previous findings, which are also reported in the Table I. Deviations with respect to reference results can be ascribed to different GW implementations and/or different DFT starting points used in the related works.⁴¹ Further details are contained in the Supplemental Material.⁶⁰

Figure 5 shows the convergence procedure for monolayer hBN, considering both the joint convergence with respect to N_b and G_{cut} (panel a), and the single-

System	$E_{gap}^{G_0W_0}$ (eV)	E_{gap}^{ref} (eV)	N_b	G_{cut} (Ry)	$\rho_{\mathbf{k}}$ (\AA^{-1})	Δ^Γ (meV)	$\Delta_{\%}^\Gamma$
Si	1.18	1.16 ⁴¹	400	16	0.33	10	0.3
Diamond	5.82	5.63 ⁶⁶	300	20	1	70	0.1
ZnO	2.36	2.35 ⁴²	800	28	0.25	10	0.4
TiO ₂	3.20	3.20 ⁴¹	600	12	0.2	10	0.3
MoS ₂	2.54	2.54 ⁶⁷	400	8	0.25	10	0.3
hBN bulk	6.28	6.30 ⁴⁰	800	20	0.25	82	1.0
hBN 2D	6.84	7.06 ⁶⁷	1200	28	0.2	42	0.5

TABLE I: G_0W_0 convergence tests on prototypical semiconductors. For each system, the minimum band gap $E_{gap}^{G_0W_0}$ (second column) is computed by using the parameters obtained by the automated convergence algorithm implemented in the `YamboConvergence` workflow, and compared with previous GW results (third column). The considered parameters are the number of empty states, N_b , the energy cutoff on the \mathbf{G} vectors, G_{cut} , and the irreducible Brillouin Zone (iBZ) \mathbf{k} -points density $\rho_{\mathbf{k}}$, expressed as the maximum distance between adjacent points along a reciprocal axis. The first two parameters are converged jointly. The last two columns include the convergence thresholds imposed on the G_0W_0 band gap at the Γ point, both in absolute (Δ^Γ) and relative ($\Delta_{\%}^\Gamma$) terms.

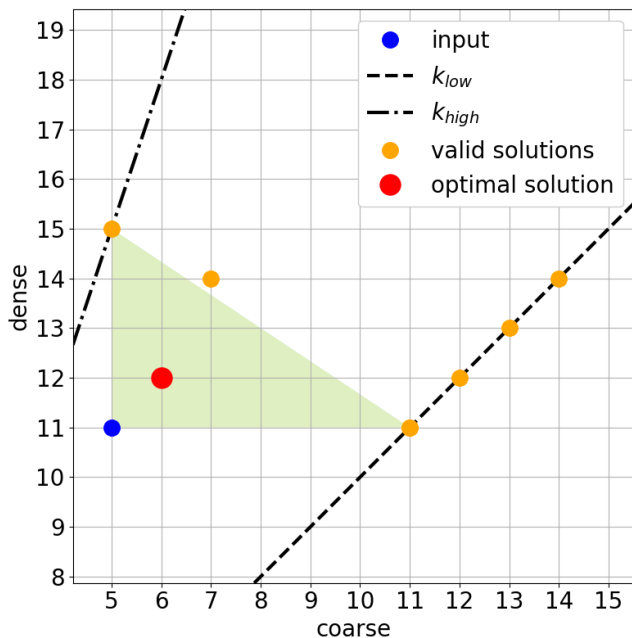


FIG. 4: **Recipe to find commensurate meshes for GW and Wannier90 calculations.** Using input meshes (11, 5) as an example, final commensurate meshes (12,6) are found. The k_{high} and k_{low} lines, that intersect in the origin, are respectively the imposed upper and lower bound for searching the commensurate meshes; the orange dots are possible solutions; the red dot is the chosen solution, which is the closest to the input in the metric of ℓ^1 norm.

parameter convergence with respect to the \mathbf{k} -mesh (panel b). Starting from an input grid with $N_b \in [200,800]$ and $G_{cut} \in [4,16]$ Ry (Figure 5a, blue shaded area), a subset of 6 calculations is performed (black squares). Since the converged guess is above the upper bound of the parameter space (see “max” variable in the plugin description), a new shifted grid (orange shaded area) is considered, and

a first guess for the converged parameters is found from the fitting procedure (blue square), now satisfying the accuracy condition (Eq. (13)a). A new fit is performed including this additional point, which results in a new converged guess (red square). The procedure is repeated till the converged result is verified to be consistent with the prediction within the given threshold (Eq. (13)a) and to be the true converged point (Eq. (13)b). A similar path is followed for the \mathbf{k} -mesh convergence (Figure 5b): a limited number of calculations is initially performed (black squares), from which the fitting is evaluated (blue curve), and the smallest grid compatible with the given threshold is finally selected (here $8 \times 8 \times 1$). We note that, despite the results of the simulations seem to have an oscillating behaviour with respect to the fitted curve, the error bar considered here (from the $14 \times 14 \times 1$ mesh) is $\sim 0.13\%$ of the band gap at Γ , i.e. ~ 10 meV, in line with the accuracy of state-of-the-art GW calculations.

The dependence of the outcome of the algorithm on the input settings (e.g., the initial value of the parameters and the boundaries of the convergence space) is a key issue for evaluating the robustness of the algorithm itself. Indeed, the convergence procedure has been tested on the starting grid for monolayer MoS₂. By using two different grids, $N_b \in [200,800]$, $G_{cut} \in [4,20]$ Ry and $N_b \in [200,1200]$, $G_{cut} \in [8,24]$ Ry, the convergence point obtained from the workflow remains the same, i.e., $(N_b, G_{cut}) = (400, 8)$. Another important issue to evaluate is the efficiency of the algorithm. We notice that, in the case of the 2D-hBN convergence shown in the left panel of Figure 5, only 14 calculations were required to reach convergence. Older implementations⁴⁹ would have required ≥ 25 simulations to achieve a final result, with over 40% reduction.

Next, the `YamboWannier90WorkChain` as been tested on bulk Si and Cu, in order to validate the automatic Wannier interpolation of GW band structures for both semiconductors and metals. Results are plotted in Fig. 6, where we compare the DFT bands, the Wannier inter-

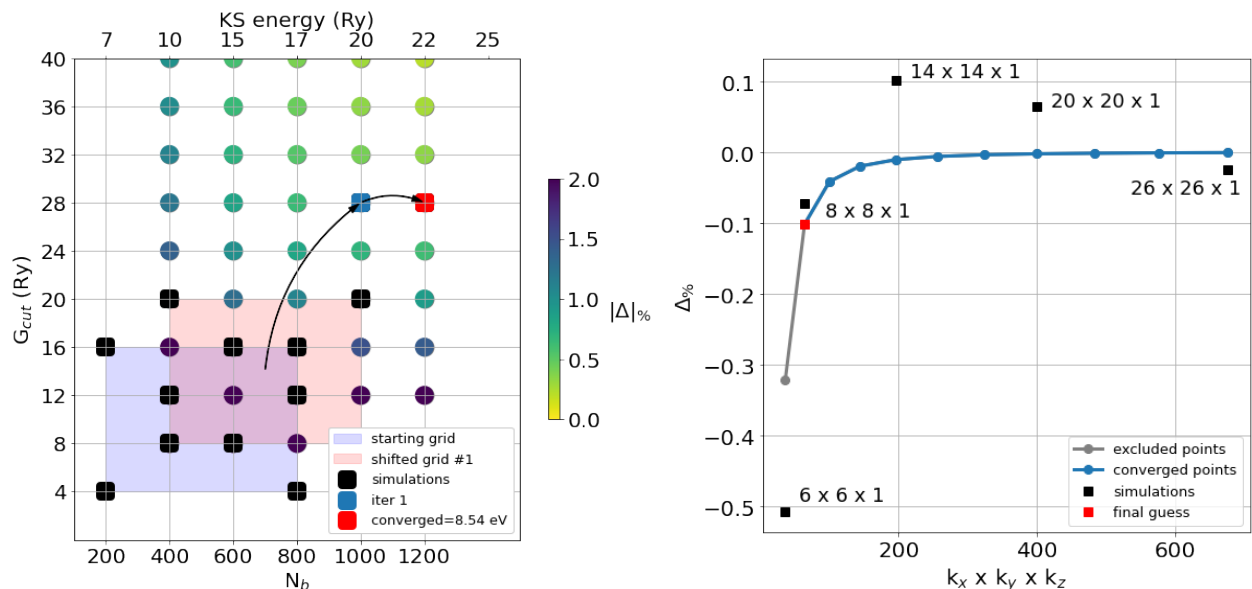


FIG. 5: **Convergence algorithm applied to monolayer hBN.** (a) Convergence of the direct quasiparticle band gap at the Γ point with respect to the coupled parameters N_b and G_{cut} . The blue shaded area represents the starting grid, while the red shaded area the shifted grid obtained after the first iteration, according to the flowchart in Fig. 1. Black squares represent the actual calculations performed by the workflow; the blue square is the first guess for the converged parameters; the red square indicates the final, converged point. The colormap specifies the relative error with respect to the converged point. A maximum absolute error of $\Delta = 42$ meV is achieved for $(N_b, G_{\text{cut}}) = (1200, 28 \text{ Ry})$, corresponding to a maximum relative error of $\Delta_{\%} = 0.5 \%$. (b) Convergence of the direct quasiparticle band gap at the Γ point with respect to the \mathbf{k} -mesh. The black points represent the actual calculations performed by the workflow, whereas the blue points are the ones obtained within the fitting procedure and used to predict the convergence. The final, converged mesh (red square) is achieved with five simulations.

polated DFT, and the Wannier interpolated GW bands. For Si (Fig. 6a), the comparison between computed and interpolated DFT bands shows that the results are almost identical, indicating the accuracy of the Wannierization of the KS wavefunctions. Moreover, the typical band gap opening upon inclusion of GW corrections is found when comparing KS and QP band structures.

For Cu (Fig. 6b), we obtain a discrepancy of ~ 10 meV around the Fermi energy (here set to zero) between computed and interpolated bands at the DFT level. Better accuracy can be achieved imposing more stringent values of the involved parameters. At QP level, the GW correction is very small around the Fermi level (~ 37 meV), but still not negligible. Here, the GW convergence is more stringent than for Si, especially concerning the \mathbf{k} -point mesh. Indeed, denser grids are needed to account for the contribution of intra-band transitions in the $\mathbf{q} \rightarrow 0$ limit, which is crucial for metallic systems but not explicitly included within the plasmon pole approximation.^{68,69} Considering the converged parameters, $(N_b, G_{\text{cut}}, \rho_{\mathbf{k}}) = (400, 18 \text{ Ry}, 0.2 \text{ \AA}^{-1})$, the quasiparticle evaluations required to interpolate the bands for the minimum converged WANNIER90 \mathbf{k} -point mesh ($16 \times 16 \times 16$) become 2900. This quite large number of QP can be easily computed using the `YamboWorkflow` workflow thanks to the possibility to split the QP calculation in several runs, each of them computing only a fraction of the GW corrections, and

then collecting all the data in a final database well-suited for the `YamboWannier90WorkChain`. Since the number of QP corrections to compute can be quite high, in the Supporting Information (section S.IIIA) we suggest an effective way to reduce the number of the required calculations for cases when accurate QP corrections are needed only in a limited energy region, e.g. around the Fermi energy, and energies outside of the chosen region can be approximated e.g. through a scissor and stretching correction.

III. CONCLUSIONS

In this work, we have presented the successful design and implementation of advanced algorithms in state-of-the-art GW (BSE) calculations, that is, convergence between interdependent parameters, error handling and automatic band interpolation by means of Wannierization. We validated the tools on selected cases among semiconductors and metallic systems. The results contained in this work clearly show the power of these newly developed workflows for the automated study of excited states properties of materials, paving the way for achieving high-throughput MBPT studies. Thanks to these developments and within the next-generation of pre-exascale and exascale supercomputers, these simulations may become

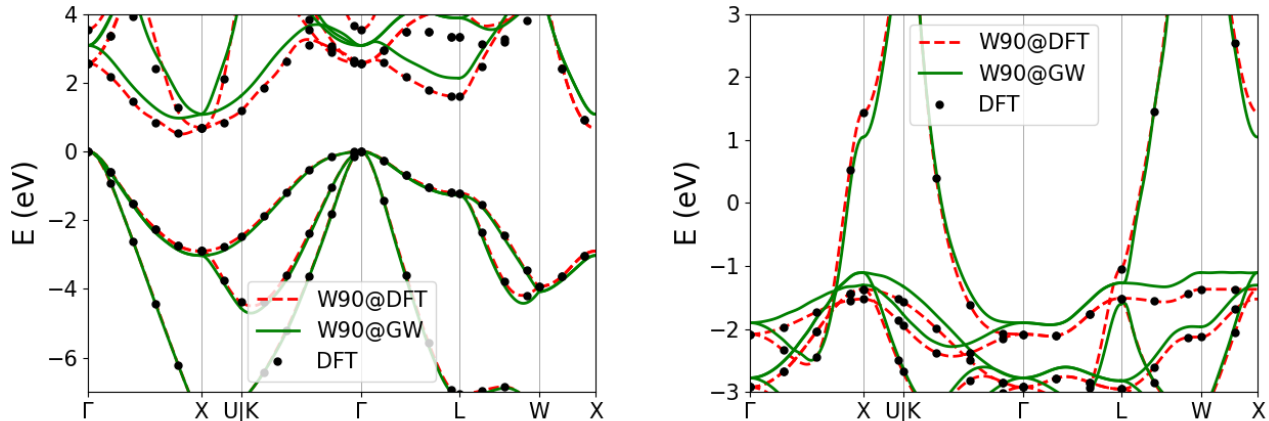


FIG. 6: **Wannier interpolation of GW band structures.** Band structure of Si (a) and Copper (b). Interpolated bands are plotted for both DFT (red dashed line) and GW (green solid line) eigenvalues, as compared to the DFT computed bands (black dots).

extensively and routinely performed by the materials-science community in the near future.

IV. METHODS

For all the systems studied here, we used symmetrized geometries in such a way to reduce the computational cost of simulations. We do not expect relevant differences in the results obtained with fully-relaxed structures. DFT simulations were carried out by using the QUANTUM ESPRESSO simulation package, which implements plane-wave basis set and pseudopotential approach. The KS-DFT exchange-correlation functional was approximated using GGA-PBE,⁷⁰ through the optimized norm-conserving Vanderbilt (ONCV) SG15^{71,72} pseudopotentials. In the case of ZnO, we adopted Local Density Approximation (LDA), to compare the results with the existing literature,^{41,42} and PseudoDojo pseudopotentials.⁷³ GW and BSE results were obtained by means of the YAMBO code. The frequency dependence of the screened interaction potential was approximated by using the Godby-Needs plasmon pole approximation⁶⁹ (GNPPA), and the quasiparticle energies were calculated according to the G_0W_0 approximation,^{53,54} as implemented in YAMBO. The Bruneval-Gonze technique⁷⁴ was used to reduce the number of empty states N_b needed for the construction of the correlation Self-Energy Σ_c (Eq. (2)). For low-dimensional systems, spurious interactions between supercell replica were avoided using a slab truncation of the Coulomb potential⁷⁵ along the non-periodic direction; its divergences are cured by means of the Random Integration Method⁷⁶ (RIM), which also accelerates convergence with respect to the BZ sampling. For 2D systems, specifically, we adopted a recently developed accelerating tech-

nique based on stochastic integration of the screened potential,⁷⁷ which allows to have GW-converged results using reduced Monkhorst-Pack \mathbf{k} -points grids, just slightly denser than the DFT one. Finally, Wannierization and band interpolations are performed by means of the WANNIER90 code. All the simulations are performed using the automated workflows implemented in the `aaiida-yambo` and `aaiida-yambo-wannier90` plugins, developed for the AiiDA platform and presented here as part of the results achieved in this work. Input parameters are generated using the protocols procedure, as implemented in the corresponding plugins.

Data availability

The data supporting the findings of this paper are available on the Materials Cloud⁷⁸ at <https://doi.org/10.24435/materialscloud:6w-qh>. Results obtained in this work can be reproduced by means of the example scripts delivered within the `aaiida-yambo` and `aaiida-yambo-wannier90` plugins.

Code availability

All the codes used in this work are fully available to the community by means of their repositories, and supported by appropriate documentations. The YAMBO code is accessible at <https://www.yambo-code.eu/download/>. The QUANTUM ESPRESSO and WANNIER90 codes can be found, respectively, at <https://www.quantum-espresso.org/download> and <http://www.wannier.org/download>.

The AiiDA infrastructure is available at <http://www.aaiida.net/download>. AiiDA plugins can be downloaded

from the corresponding GitHub repositories, already referenced throughout the manuscript, see Refs. 61,64.

Acknowledgements

We acknowledge stimulating discussions with Nicola Marzari, Michael O. Atambo, Gianluca Prandini, Dario A. L. Valido, Alberto Guandalini and Fulvio Paleari. This work was supported by: MaX – MAterials design at the eXascale – a European Centre of Excellence funded by the European Union’s program H2020-INFRAEDI-2018-1 (Grant No. 824143); the European Union’s Horizon 2020 research and innovation programme (Grant No. 957189, BIG-MAP, also part of the BATTERY 2030+ initiative, Grant No. 957213); SUPER (Supercomputing Unified Platform – Emilia-Romagna) from Emilia-Romagna PORFESR 2014-2020 regional funds; the Swiss National Science Foundation (SNSF) Project Funding (Grant No. 200021E.206190 “FISH4DIET”); NCCR

MARVEL, a National Centre of Competence in Research, funded by the Swiss National Science Foundation (Grant No. 205602). Computational time on the Marconi100 and Galileo100 machines at CINECA was provided by the Italian ISCR program.

Author contributions

M.B., J.Q., A.M. and N.S. contributed to the development of the `aiida-yambo` plugin; M.B. designed, implemented and tested the automatic convergence algorithm, and the other workflows belonging to the `aiida-yambo` plugin. J.Q. and M.B. implemented the `aiida-yambo-wannier90` plugin. E.M., A.F., D.V., D.P, G.P. were responsible for the project supervision and coordination. M.B., J.Q., and D.P. wrote the manuscript with contributions from all authors.

The Authors declare no Competing Financial or Non-Financial Interests

* corresponding author: miki.bonacci@nano.cnr.it

- ¹ S. Curtarolo, G. L. W. Hart, M. B. Nardelli, N. Mingo, S. Sanvito, and O. Levy, *The high-throughput highway to computational materials design*, *Nature Materials* **12**, 191 (2013).
- ² K. S. Vecchio, O. F. Dippo, K. R. Kaufmann, and X. Liu, *High-throughput rapid experimental alloy development (HT-READ)*, *Acta Materialia* **221**, 117352 (2021).
- ³ S. Luo, T. Li, X. Wang, M. Faizan, and L. Zhang, *High-throughput computational materials screening and discovery of optoelectronic semiconductors*, *WIREs Computational Molecular Science* **11** (2021).
- ⁴ M. Ashton, J. Paul, S. B. Sinnott, and R. G. Hennig, *Topology-Scaling Identification of Layered Solids and Stable Exfoliated 2D Materials*, *Physical Review Letters* **118**, 106101 (2017).
- ⁵ G. Cheon, K.-A. N. Duerloo, A. D. Sendek, C. Porter, Y. Chen, and E. J. Reed, *Data Mining for New Two- and One-Dimensional Weakly Bonded Solids and Lattice-Commensurate Heterostructures*, *Nano Letters* **17**, 1915 (2017).
- ⁶ N. Mounet, M. Gibertini, P. Schwaller, D. Campi, A. Merkys, A. Marrazzo, T. Sohier, I. E. Castelli, A. Cepellotti, G. Pizzi, and et al., *Two-dimensional materials from high-throughput computational exfoliation of experimentally known compounds*, *Nature Nanotechnology* **13**, 246–252 (2018).
- ⁷ K. Choudhary, I. Kalish, R. Beams, and F. Tavazza, *High-throughput Identification and Characterization of Two-dimensional Materials using Density functional theory*, *Scientific Reports* **7**, 5179 (2017).
- ⁸ N. Mounet, M. Gibertini, P. Schwaller, D. Campi, A. Merkys, A. Marrazzo, T. Sohier, I. E. Castelli, A. Cepellotti, and G. Pizzi, *Two-dimensional materials from high-throughput computational exfoliation of experimentally known compounds*, *Materials Cloud Archive* **2020.158** (2020).

- ⁹ S. Haastруп, M. Strange, M. Pandey, T. Deilmann, P. S. Schmidt, N. F. Hinsche, M. N. Gjerding, D. Torelli, P. M. Larsen, A. C. Riis-Jensen, J. Gath, K. W. Jacobsen, J. Jørgen Mortensen, T. Olsen, and K. S. Thygesen, *The Computational 2D Materials Database: high-throughput modeling and discovery of atomically thin crystals*, *2D Materials* **5**, 042002 (2018).
- ¹⁰ A. Marrazzo, M. Gibertini, D. Campi, N. Mounet, and N. Marzari, *Relative Abundance of Z2 Topological Order in Exfoliable Two-Dimensional Insulators*, *Nano Letters* **19**, 8431 (2019).
- ¹¹ S. Kirklin, B. Meredig, and C. Wolverton, *High-Throughput Computational Screening of New Li-Ion Battery Anode Materials*, *Advanced Energy Materials* **3**, 252 (2013).
- ¹² Z. Zhang, X. Zhang, X. Zhao, S. Yao, A. Chen, and Z. Zhou, *Computational Screening of Layered Materials for Multivalent Ion Batteries*, *ACS Omega* **4**, 7822 (2019).
- ¹³ W. Chen, J.-H. Pöhls, G. Hautier, D. Broberg, S. Bajaj, U. Aydemir, Z. M. Gibbs, H. Zhu, M. Asta, G. J. Snyder, B. Meredig, M. A. White, K. Persson, and A. Jain, *Understanding thermoelectric properties from high-throughput calculations: trends, insights, and comparisons with experiment*, *Journal of Materials Chemistry C* **4**, 4414 (2016).
- ¹⁴ S. Bhattacharya and G. K. H. Madsen, *High-throughput exploration of alloying as design strategy for thermoelectrics*, *Physical Review B* **92**, 085205 (2015).
- ¹⁵ I. E. Castelli, T. Olsen, S. Datta, D. D. Landis, S. Dahl, K. S. Thygesen, and K. W. Jacobsen, *Computational screening of perovskite metal oxides for optimal solar light capture*, *Energy Environ. Sci.* **5**, 5814 (2012).
- ¹⁶ L. Yu and A. Zunger, *Identification of Potential Photovoltaic Absorbers Based on First-Principles Spectroscopic Screening of Materials*, *Physical Review Letters* **108**, 068701 (2012).
- ¹⁷ Q. Yan, J. Yu, S. K. Suram, L. Zhou, A. Shinde, P. F. Newhouse, W. Chen, G. Li, K. A. Persson, J. M. Gre-

- goire, and J. B. Neaton, *Solar fuels photoanode materials discovery by integrating high-throughput theory and experiment*, Proceedings of the National Academy of Sciences **114**, 3040 (2017).
- ¹⁸ K. Kuhar, M. Pandey, K. S. Thygesen, and K. W. Jacobsen, *High-Throughput Computational Assessment of Previously Synthesized Semiconductors for Photovoltaic and Photoelectrochemical Devices*, ACS Energy Letters **3**, 436 (2018).
- ¹⁹ K. Lejaeghere, G. Bihlmayer, T. Björkman, P. Blaha, S. Blügel, V. Blum, D. Caliste, I. E. Castelli, S. J. Clark, A. Dal Corso, S. de Gironcoli, T. Deutsch, J. K. Dewhurst, I. Di Marco, C. Draxl, M. Dulak, O. Eriksson, J. A. Flores-Livas, K. F. Garrity, L. Genovese, P. Giannozzi, M. Giantomassi, S. Goedecker, X. Gonze, O. Grånäs, E. K. U. Gross, A. Gulans, F. Gygi, D. R. Hamann, P. J. Hasnip, N. A. W. Holzwarth, D. Iușan, D. B. Jochym, F. Jollet, D. Jones, G. Kresse, K. Koepnik, E. Küçükbenli, Y. O. Kvashnin, I. L. M. Locht, S. Lubeck, M. Marsman, N. Marzari, U. Nitzsche, L. Nordström, T. Ozaki, L. Paulatto, C. J. Pickard, W. Poelmans, M. I. J. Probert, K. Refson, M. Richter, G.-M. Rignanese, S. Saha, M. Scheffler, M. Schlipf, K. Schwarz, S. Sharma, F. Tavazza, P. Thunström, A. Tkatchenko, M. Torrent, D. Vanderbilt, M. J. van Setten, V. Van Speybroeck, J. M. Wills, J. R. Yates, G.-X. Zhang, and S. Cottenier, *Reproducibility in density functional theory calculations of solids*, Science **351**, aad3000 (2016).
- ²⁰ G. Prandini, A. Marrazzo, I. E. Castelli, N. Mounet, and N. Marzari, *Precision and efficiency in solid-state pseudopotential calculations*, npj Computational Materials **4**, 72 (2018).
- ²¹ S. Maffioletti and R. Murri, *GC3Pie: A Python framework for high-throughput computing*, in *Proceedings of EGI Community Forum 2012 / EMI Second Technical Conference — PoS(EGICF12-EMITC2)*, page 143, Munich, Germany, 2012, Sissa Medialab.
- ²² S. Curtarolo, W. Setyan, G. L. Hart, M. Jahnatek, R. V. Chepulskii, R. H. Taylor, S. Wang, J. Xue, K. Yang, O. Levy, M. J. Mehl, H. T. Stokes, D. O. Demchenko, and D. Morgan, *AFLOW: An automatic framework for high-throughput materials discovery*, Computational Materials Science **58**, 218 (2012).
- ²³ A. Jain, S. P. Ong, W. Chen, B. Medasani, X. Qu, M. Kocher, M. Brafman, G. Petretto, G. Rignanese, G. Hautier, D. Gunter, and K. A. Persson, *FireWorks: a dynamic workflow system designed for high-throughput applications*, Concurrency and Computation: Practice and Experience **27**, 5037 (2015).
- ²⁴ G. Pizzi, A. Cepellotti, R. Sabatini, N. Marzari, and B. Kozinsky, *AiiDA: automated interactive infrastructure and database for computational science*, Comput. Mater. Sci. **111**, 218 (2016).
- ²⁵ A. Hjorth Larsen, J. Jørgen Mortensen, J. Blomqvist, I. E. Castelli, R. Christensen, M. Dulak, J. Friis, M. N. Groves, B. Hammer, C. Hargus, E. D. Hermes, P. C. Jennings, P. Bjerre Jensen, J. Kermode, J. R. Kitchin, E. Leonhard Kolsbjerg, J. Kubal, K. Kaasbjerg, S. Lysgaard, J. Bergmann Maronsson, T. Maxson, T. Olsen, L. Pastewka, A. Peterson, C. Rostgaard, J. Schiøtz, O. Schütt, M. Strange, K. S. Thygesen, T. Vegge, L. Vilhelmsen, M. Walter, Z. Zeng, and K. W. Jacobsen, *The atomic simulation environment—a Python library for working with atoms*, Journal of Physics: Condensed Matter **29**, 273002 (2017).
- ²⁶ K. Mathew, J. H. Montoya, A. Faghaninia, S. Dwarakanath, M. Aykol, H. Tang, I.-h. Chu, T. Smidt, B. Bocklund, M. Horton, J. Dagdelen, B. Wood, Z.-K. Liu, J. Neaton, S. P. Ong, K. Persson, and A. Jain, *Atomate: A high-level interface to generate, execute, and analyze computational materials science workflows*, Computational Materials Science **139**, 140 (2017).
- ²⁷ J. Mortensen, M. Gjerding, and K. Thygesen, *MyQueue: Task and workflow scheduling system*, Journal of Open Source Software **5**, 1844 (2020).
- ²⁸ S. P. Huber, S. Zoupanos, M. Uhrin, L. Talirz, L. Kahle, R. Häuselmann, D. Gresch, T. Müller, A. V. Yakutovich, C. W. Andersen, F. F. Ramirez, C. S. Adorf, F. Gargiulo, S. Kumbhar, E. Passaro, C. Johnston, A. Merkys, A. Cepellotti, N. Mounet, N. Marzari, B. Kozinsky, and G. Pizzi, *AiiDA 1.0, a scalable computational infrastructure for automated reproducible workflows and data provenance*, Sci. Data **7**, 300 (2020).
- ²⁹ M. Uhrin, S. P. Huber, J. Yu, N. Marzari, and G. Pizzi, *Workflows in AiiDA: Engineering a high-throughput, event-based engine for robust and modular computational workflows*, Comp. Mat. Sci. **187**, 110086 (2021).
- ³⁰ A. Bablich, S. Kataria, and M. C. Lemme, *Graphene and Two-Dimensional Materials for Optoelectronic Applications*, Electronics **5** (2016).
- ³¹ X. Zhang, J. Shao, C. Yan, R. Qin, Z. Lu, H. Geng, T. Xu, and L. Ju, *A review on optoelectronic device applications of 2D transition metal carbides and nitrides*, Materials and Design **200**, 109452 (2021).
- ³² J. Jean, P. R. Brown, R. L. Jaffe, T. Buonassisi, and V. Bulović, *Pathways for solar photovoltaics*, Energy Environ. Sci. **8**, 1200 (2015).
- ³³ S. Zhu and D. Wang, *Photocatalysis: Basic Principles, Diverse Forms of Implementations and Emerging Scientific Opportunities*, Adv. En. Mater. **7**, 1700841 (2017).
- ³⁴ W. Jin and L. Hu, *Review on Quasi One-Dimensional CdSe Nanomaterials: Synthesis and Application in Photodetectors*, Nanomaterials **9** (2019).
- ³⁵ F. Xia, T. Mueller, Y.-m. Lin, A. Valdes-Garcia, and P. Avouris, *Ultrafast graphene photodetector*, Nature Nanotechnology **4**, 839 (2009).
- ³⁶ W. Lee, S. Ha, H. Lee, J. Bae, B. Jang, H. Kwon, Y. Yun, S. Lee, and J. Jang, *High-Detectivity Flexible Near-Infrared Photodetector Based on Chalcogenide Ag₂Se Nanoparticles*, Advanced Optical Materials **7**, 1900812 (2019).
- ³⁷ R. M. Martin, L. Reining, and D. M. Ceperley, *Interacting Electrons: Theory and Computational Approaches*, Cambridge University Press, 2016.
- ³⁸ M. J. van Setten, M. Giantomassi, X. Gonze, G.-M. Rignanese, and G. Hautier, *Automation methodologies and large-scale validation for GW: Towards high-throughput GW calculations*, Physical Review B **96**, 155207 (2017).
- ³⁹ A. Rasmussen, T. Deilmann, and K. S. Thygesen, *Towards fully automated GW band structure calculations: What we can learn from 60.000 self-energy evaluations*, npj Computational Materials **7**, 22 (2021).
- ⁴⁰ F. Hüser, T. Olsen, and K. S. Thygesen, *Quasiparticle GW calculations for solids, molecules, and two-dimensional materials*, Physical Review B **87**, 235132 (2013).
- ⁴¹ T. Rangel, M. Del Ben, D. Varsano, G. Antonius, F. Bruneval, F. H. da Jornada, M. J. van Setten, O. K. Orhan, D. D. O’Regan, A. Canning, A. Ferretti, A. Marini, G.-M. Rignanese, J. Deslippe, S. G. Louie, and J. B.

- Neaton, *Reproducibility in $G0W0$ calculations for solids*, Computer Physics Communications **255**, 107242 (2020).
- ⁴² M. Stankovski, G. Antonius, D. Waroquiers, A. Miglio, H. Dixit, K. Sankaran, M. Giantomassi, X. Gonze, M. Côté, and G.-M. Rignanese, *$G0W0$ band gap of ZnO: Effects of plasmon-pole models*, Physical Review B **84**, 241201 (2011).
- ⁴³ R. Mercado, R.-S. Fu, A. V. Yakutovich, L. Talirz, M. Haracznyk, and B. Smit, *In Silico Design of 2D and 3D Covalent Organic Frameworks for Methane Storage Applications*, Chemistry of Materials **30**, 5069 (2018).
- ⁴⁴ G. Prandini, A. Marrazzo, I. E. Castelli, N. Mounet, and N. Marzari, *Precision and efficiency in solid-state pseudopotential calculations*, npj Computational Materials **4**, 72 (2018).
- ⁴⁵ V. Vitale, G. Pizzi, A. Marrazzo, J. R. Yates, N. Marzari, and A. A. Mostofi, *Automated high-throughput Wannierization*, npj Comput. Mater. **6**, 66 (2020).
- ⁴⁶ P. Giannozzi, S. Baroni, N. Bonini, M. Calandra, R. Car, C. Cavazzoni, D. Ceresoli, G. L. Chiarotti, M. Cococcioni, I. Dabo, A. Dal Corso, S. de Gironcoli, S. Fabris, G. Fratesi, R. Gebauer, U. Gerstmann, C. Gougousis, A. Kokalj, M. Lazzeri, L. Martin-Samos, N. Marzari, F. Mauri, R. Mazzarello, S. Paolini, A. Pasquarello, L. Paulatto, C. Sbraccia, S. Scandolo, G. Sclauzero, A. P. Seitsonen, A. Smogunov, P. Umari, and R. M. Wentzcovitch, *QUANTUM ESPRESSO: a modular and open-source software project for quantum simulations of materials*, J. Phys.: Condens. Matter **21**, 395502 (2009).
- ⁴⁷ P. Giannozzi, O. Andreussi, T. Brumme, O. Bunau, M. Buongiorno Nardelli, M. Calandra, R. Car, C. Cavazzoni, D. Ceresoli, M. Cococcioni, N. Colonna, I. Carnimeo, A. Dal Corso, S. de Gironcoli, P. Delugas, J. DiStasio, R. A., A. Ferretti, A. Floris, G. Fratesi, G. Fugallo, R. Gebauer, U. Gerstmann, F. Giustino, T. Gorni, J. Jia, M. Kawamura, H. Y. Ko, A. Kokalj, E. Küçükbenli, M. Lazzeri, M. Marsili, N. Marzari, F. Mauri, N. L. Nguyen, H. V. Nguyen, A. Otero-de-la-Roza, L. Paulatto, S. Poncé, D. Rocca, R. Sabatini, B. Santra, M. Schlipf, A. P. Seitsonen, A. Smogunov, I. Timrov, T. Thonhauser, P. Umari, N. Vast, X. Wu, and S. Baroni, *Advanced capabilities for materials modelling with Quantum ESPRESSO*, J. Phys.: Condens. Matter **29**, 465901 (2017).
- ⁴⁸ A. Marini, C. Hogan, M. Grüning, and D. Varsano, *yambo: An ab initio tool for excited state calculations*, Comput. Phys. Commun. **180**, 1392 (2009).
- ⁴⁹ D. Sangalli, A. Ferretti, H. Miranda, C. Attaccalite, I. Marri, E. Cannuccia, P. Melo, M. Marsili, F. Paleari, A. Marrazzo, G. Prandini, P. Bonfà, M. O. Atambo, F. Affinito, M. Palumbo, A. Molina-Sánchez, C. Hogan, M. Grüning, D. Varsano, and A. Marini, *Many-body perturbation theory calculations using the yambo code*, J. Phys.: Condens. Matter **31**, 325902 (2019).
- ⁵⁰ N. Marzari, A. A. Mostofi, J. R. Yates, I. Souza, and D. Vanderbilt, *Maximally localized Wannier functions: Theory and applications*, Reviews of Modern Physics **84**, 1419 (2012).
- ⁵¹ G. Pizzi, V. Vitale, R. Arita, S. Blügel, F. Freimuth, G. Géranton, M. Gibertini, D. Gresch, C. Johnson, T. Koretsune, J. Ibañez-Azpiroz, H. Lee, J.-M. Lihm, D. Marchand, A. Marrazzo, Y. Mokrousov, J. I. Mustafa, Y. Nohara, Y. Nomura, L. Paulatto, S. Poncé, T. Ponce, J. Qiao, F. Thöle, S. S. Tsirkin, M. Wierzbowska, N. Marzari, D. Vanderbilt, I. Souza, A. A. Mostofi, and J. R. Yates, *Wannier90 as a community code: new features and applications*, Journal of Physics: Condensed Matter **32**, 165902 (2020).
- ⁵² A. V. Yakutovich, K. Eimre, O. Schütt, L. Talirz, C. S. Adorf, C. W. Andersen, E. Ditle, D. Du, D. Passerone, B. Smit, N. Marzari, G. Pizzi, and C. A. Pignedoli, *AiidaLab – an ecosystem for developing, executing, and sharing scientific workflows*, Computational Materials Science **188**, 110165 (2021).
- ⁵³ L. Hedin, *New Method for Calculating the One-Particle Green's Function with Application to the Electron-Gas Problem*, Phys. Rev. **139**, 796 (1965).
- ⁵⁴ G. Onida, L. Reining, and A. Rubio, *Electronic excitations: density-functional versus many-body Green's-function approaches*, Rev. Mod. Phys. **74**, 601 (2002).
- ⁵⁵ W. Gao, W. Xia, X. Gao, and P. Zhang, *Speeding up GW Calculations to Meet the Challenge of Large Scale Quasiparticle Predictions*, Scientific Reports **6**, 36849 (2016).
- ⁵⁶ G. Strinati, *Application of the Green's functions method to the study of the optical properties of semiconductors*, La Rivista del Nuovo Cimento (1978-1999) **11**, 1 (1988).
- ⁵⁷ A. Schindlmayr, *Analytic evaluation of the electronic self-energy in the GW approximation for two electrons on a sphere*, Physical Review B **87**, 075104 (2013).
- ⁵⁸ J. Klimeš, M. Kaltak, and G. Kresse, *Predictive GW calculations using plane waves and pseudopotentials*, Physical Review B **90**, 075125 (2014).
- ⁵⁹ E. Maggio, P. Liu, M. J. van Setten, and G. Kresse, *GW100: A Plane Wave Perspective for Small Molecules*, Journal of Chemical Theory and Computation **13**, 635 (2017), PMID: 28094981.
- ⁶⁰ See Supplemental Material for details on the older convergence algorithm, convergence plots obtained within this work and additional information in the Wannierization steps.
- ⁶¹ The `aiida-yambo` code is available at <https://github.com/yambo-code/aiida-yambo>.
- ⁶² S. P. Huber, E. Bosoni, M. Bercx, J. Bröder, A. Degomme, V. Dikan, K. Eimre, E. Flage-Larsen, A. Garcia, L. Genovese, D. Gresch, C. Johnston, G. Petretto, S. Poncé, G.-M. Rignanese, C. J. Sewell, B. Smit, V. Tseplyaev, M. Uhrin, D. Wortmann, A. V. Yakutovich, A. Zadoks, P. Zarabadi-Poor, B. Zhu, N. Marzari, and G. Pizzi, *Common workflows for computing material properties using different quantum engines*, npj Computational Materials **7**, 136 (2021).
- ⁶³ The `aiida-yambo` documentation is available at <https://aiida-yambo.readthedocs.io/en/master/>.
- ⁶⁴ The `aiida-yambo-wannier90` code is available at <https://github.com/aiidaplugins/aiida-yambo-wannier90>.
- ⁶⁵ The `aiida-yambo-wannier90` documentation is available at <https://aiida-yambo-wannier90.readthedocs.io/en/latest/>.
- ⁶⁶ S.-P. Gao, *Band gaps and dielectric functions of cubic and hexagonal diamond polytypes calculated by many-body perturbation theory*, physica status solidi (b) **252**, 235 (2015).
- ⁶⁷ F. A. Rasmussen, P. S. Schmidt, K. T. Winther, and K. S. Thygesen, *Efficient many-body calculations for two-dimensional materials using exact limits for the screened potential: Band gaps of MoS_2 , h -BN, and phosphorene*, Phys. Rev. B **94**, 155406 (2016).
- ⁶⁸ M. S. Hybertsen and S. G. Louie, *Electron correlation in semiconductors and insulators: Band gaps and quasiparticle energies*, Phys. Rev. B **34**, 5390 (1986).

- ⁶⁹ R. W. Godby and R. J. Needs, *Metal-insulator transition in Kohn-Sham theory and quasiparticle theory*, Phys. Rev. Lett. **62**, 1169 (1989).
- ⁷⁰ J. P. Perdew, K. Burke, and M. Ernzerhof, *Generalized Gradient Approximation Made Simple*, Phys. Rev. Lett. **77**, 3865 (1996).
- ⁷¹ D. R. Hamann, *Optimized norm-conserving Vanderbilt pseudopotentials*, Phys. Rev. B **88**, 085117 (2013).
- ⁷² M. Schlipf and F. Gygi, *Optimization algorithm for the generation of ONCV pseudopotentials*, Computer Physics Communications **196**, 36 (2015).
- ⁷³ M. van Setten, M. Giantomassi, E. Bousquet, M. Verstraete, D. Hamann, X. Gonze, and G.-M. Rignanese, *The PseudoDojo: Training and grading a 85 element optimized norm-conserving pseudopotential table*, Computer Physics Communications **226**, 39 (2018).
- ⁷⁴ F. Bruneval and X. Gonze, *Accurate $G W$ self-energies in a plane-wave basis using only a few empty states: Towards large systems*, Physical Review B **78**, 085125 (2008).
- ⁷⁵ C. A. Rozzi, D. Varsano, A. Marini, E. K. U. Gross, and A. Rubio, *Exact Coulomb cutoff technique for supercell calculations*, Phys. Rev. B **73**, 205119 (2006).
- ⁷⁶ O. Pulci, G. Onida, R. Del Sole, and L. Reining, *Ab Initio Calculation of Self-Energy Effects on Optical Properties of GaAs(110)*, Physical Review Letters **81**, 5374 (1998).
- ⁷⁷ A. Guandalini, P. D'Amico, A. Ferretti, and D. Varsano, *Efficient GW calculations in two dimensional materials through a stochastic integration of the screened potential*, 2022.
- ⁷⁸ L. Talirz, S. Kumbhar, E. Passaro, A. V. Yakutovich, V. Granata, F. Gargiulo, M. Borelli, M. Uhrin, S. P. Huber, S. Zoupanos, C. S. Adorf, C. W. Andersen, O. Schütt, C. A. Pignedoli, D. Passerone, J. VandeVondele, T. C. Schulthess, B. Smit, G. Pizzi, and N. Marzari, *Materials Cloud, a platform for open computational science*, Scientific Data **7**, 299 (2020).
- ⁷⁹ According to our experience, the asymptotic region can be safely identified by choosing $\Delta_i = 5 \cdot 10^{-5}$ and $\Delta_{ij} = 1 \cdot 10^{-8}$.
- ⁸⁰ The output parsing of the `aiida-yambo` plugin is partially done by using `YAMBOPY` functions.⁴⁹

Supplementary Material for: Towards high-throughput many-body perturbation theory: efficient algorithms and automated workflows

Miki Bonacci,^{1,2,*} Junfeng Qiao,³ Nicola Spallanzani,² Antimo Marrazzo,⁴ Giovanni Pizzi,^{3,5} Elisa Molinari,^{1,2} Daniele Varsano,² Andrea Ferretti,² and Deborah Prezzi²

¹FIM Department, University of Modena and Reggio Emilia, Via Campi 213/a, Modena, Italy

²S3 Center, Istituto Nanoscienze, CNR, Via Campi 213/a, Modena, Italy

³Theory and Simulation of Materials (THEOS) and National Centre for Computational Design and Discovery of Novel Materials (MARVEL),

École Polytechnique Fédérale de Lausanne, CH-1015 Lausanne, Switzerland

⁴Dipartimento di Fisica, Università di Trieste, I-34151 Trieste, Italy

⁵Laboratory for Materials Simulations (LMS), Paul Scherrer Institut (PSI), CH-5232 Villigen PSI, Switzerland

I. CONVERGENCE PLOTS FOR THE SYSTEMS STUDIED IN THIS WORK

In the following, we show the convergence plot for the systems studied in this work, as done in the main text for the monolayer hBN case. We converged the $\Gamma - \Gamma$ band gap with respect to the two coupled parameters N_b and G_{cut} and the \mathbf{k} -point grid as well, except for TiO_2 and ZnO . For diamond, we converged also the FFTGvecs parameter, governing the Fast-Fourier-Transform (FFT) size for the evaluation of the generalized dipole matrix elements.

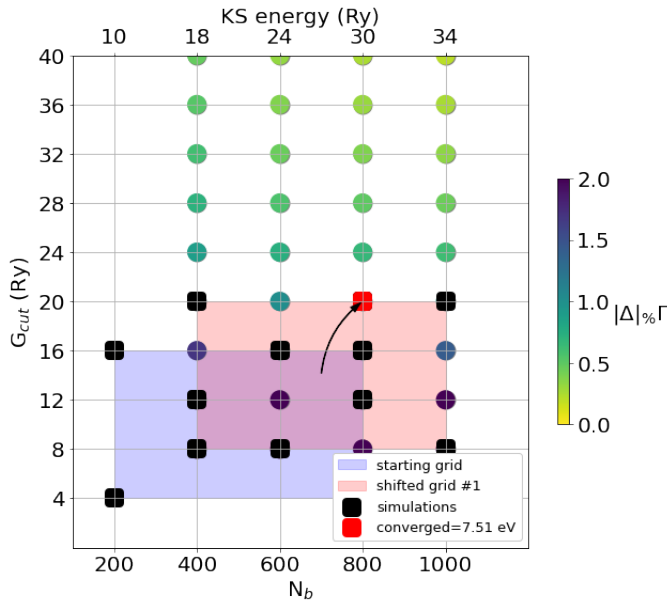


FIG. 1: Convergence of N_b and G_{cut} for bulk hBN.

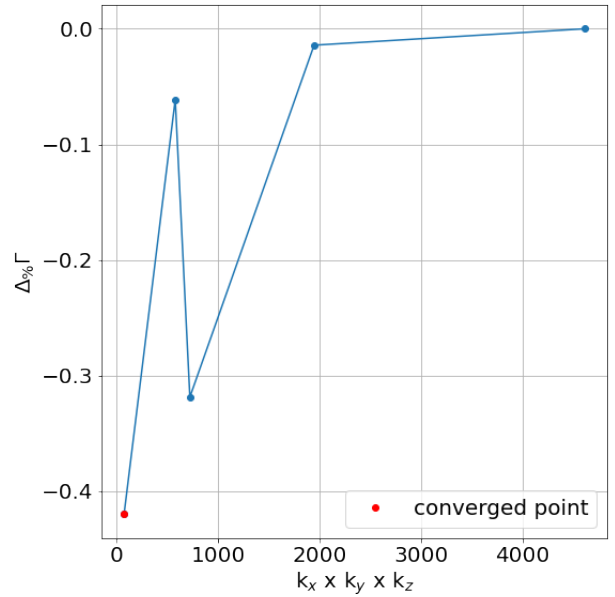
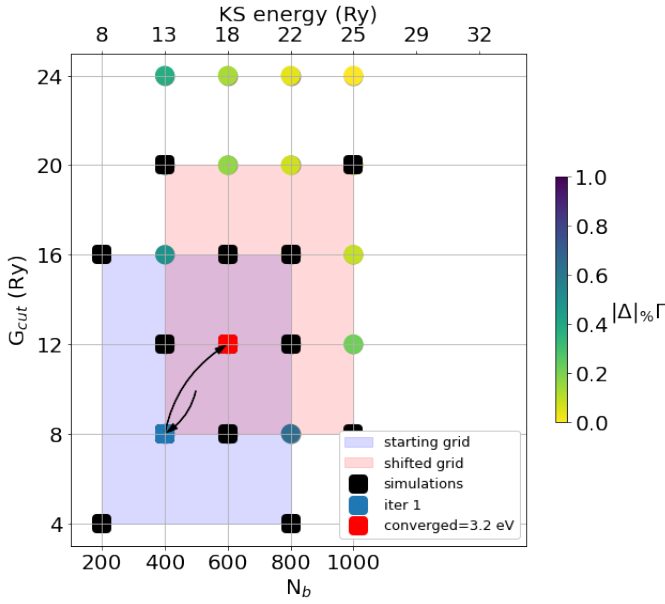
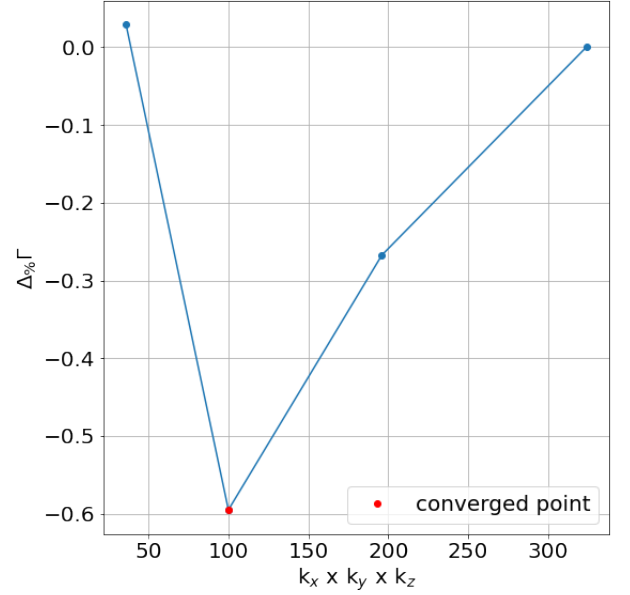
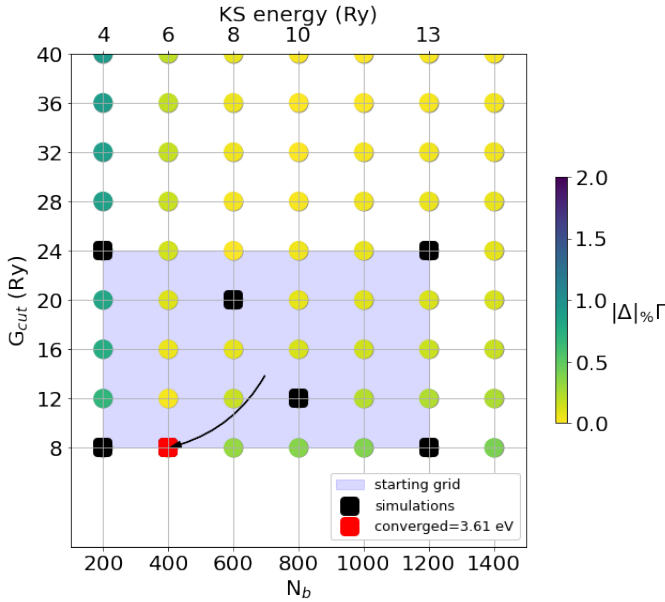
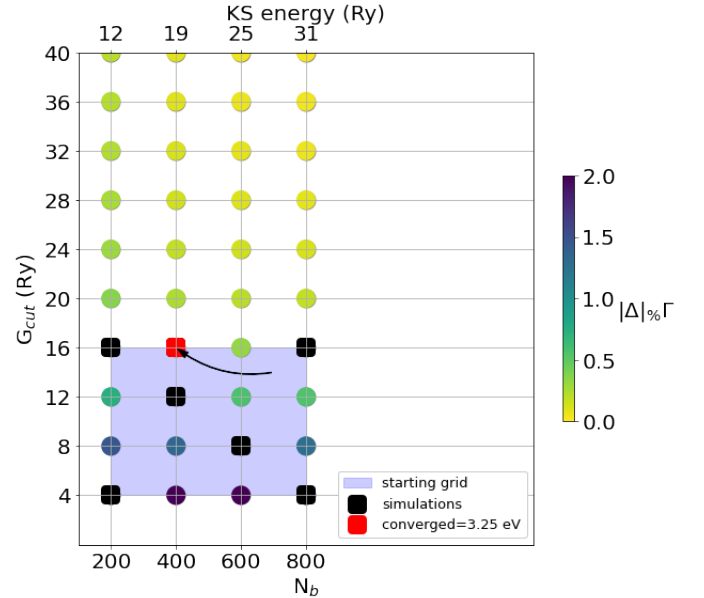


FIG. 2: k-mesh convergence for bulk hBN.

II. WANNIERIZATION AT THE GW LEVEL AND RESTART FROM DFT WANNIERIZATION

Figure 12 shows a detailed flowchart of the Wannierization workflow for GW band structure. The right column shows further details of Wannierization with respect to the ones provided in the main text. Firstly, a `Wannier90Calculation` is launched to generate the `nkp` file for the subsequent `YppRestart`, which performs the `ypp` calculation for writing the QP correction in the `eig` file format for `Wannier90`. Then, a `Wannier90BandsWorkChain` is launched for Wannier interpolated bands at DFT level. Next, a `Gw2wannier90Calculation` sorts the new eigenenergies in ascending order, and rewrites relevant files. Finally, a `Wannier90BaseWorkChain` is launched to obtain the Wannier interpolated bands at G_0W_0 level.

Some special care need to be taken at the step of incorporating the GW correction to the `Wannier90` inputs, i.e., the initial projection matrices $A_{m\mathbf{k}}$, the overlap ma-

FIG. 3: Convergence of N_b and G_{cut} for Rutile TiO_2 .FIG. 5: \mathbf{k} -mesh convergence for monolayer MoS_2 .FIG. 4: Convergence of N_b and G_{cut} for monolayer MoS_2 .FIG. 6: Convergence of N_b and G_{cut} for silicon.

trices $M_{mn\mathbf{k}\mathbf{b}}$, the eigenvalues $\epsilon_{n\mathbf{k}}$, and the Bloch wavefunctions $|u_{n\mathbf{k}}\rangle$, where the \mathbf{b} is the \mathbf{b} vectors connecting neighboring \mathbf{k} points.[?] Since the GW correction might change the order of eigenvalues, and the Wannierization disentangling process requires the eigenvalues to be sorted in ascending order, we need to sort the GW corrected eigenenergies and rewrite the $A_{mn\mathbf{k}}$, $M_{mn\mathbf{k}\mathbf{b}}$, and $|u_{n\mathbf{k}}\rangle$ files accordingly. Then the Wannierization and interpolation proceed as usual. Another option is reusing the unitary transformation matrices $U_{mn\mathbf{k}}$ from the Wannierization at DFT level. Since the G_0W_0 only corrects

energies, while the wavefunctions are left unchanged, it is expected that the orbital characters of the wavefunctions are unchanged, thus the disentangling process should still choose the same set of orbitals, i.e., the previous $U_{mn\mathbf{k}}$ should work as well for the G_0W_0 corrections. Therefore, we can also reuse the $U_{mn\mathbf{k}}$ for the Wannier interpolation of G_0W_0 eigenenergies thus skipping the second disentangling step. The Wannier interpolation is the inverse Fourier transform of the Hamiltonian on the \mathbf{k} point path for the band structure, the order of eigenenergies is irrelevant, thus the $A_{mn\mathbf{k}}$, $M_{mn\mathbf{k}\mathbf{b}}$, and $|u_{n\mathbf{k}}\rangle$

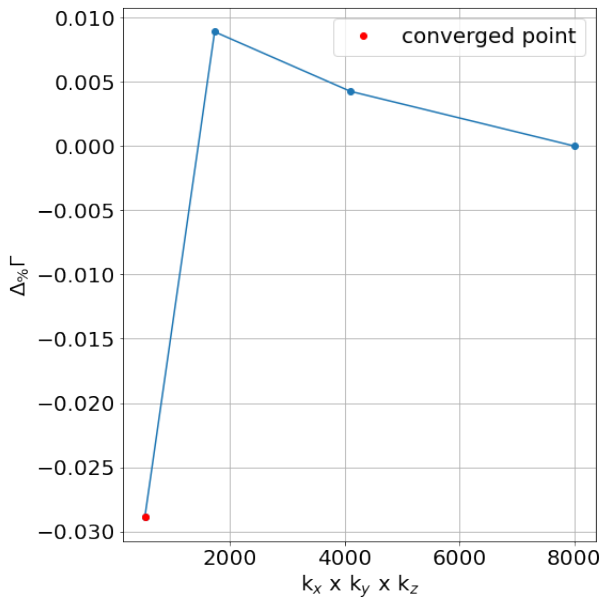
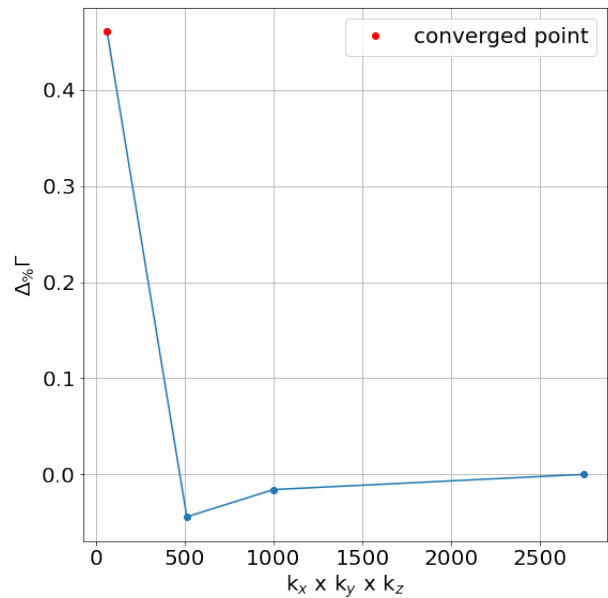
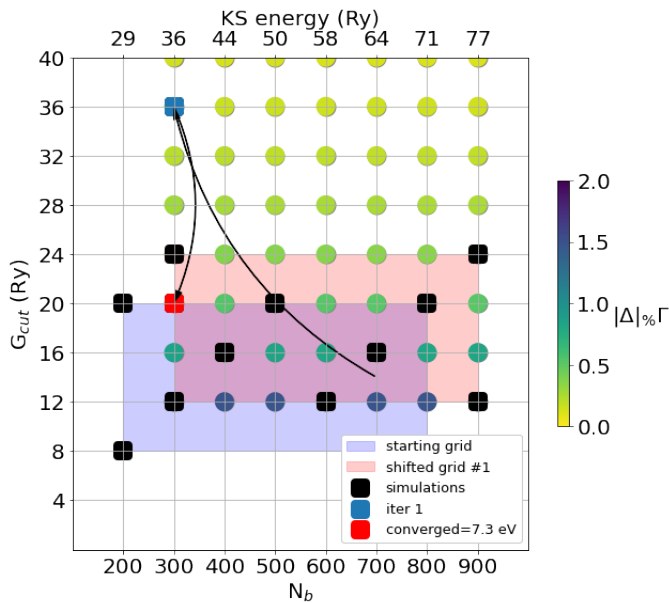
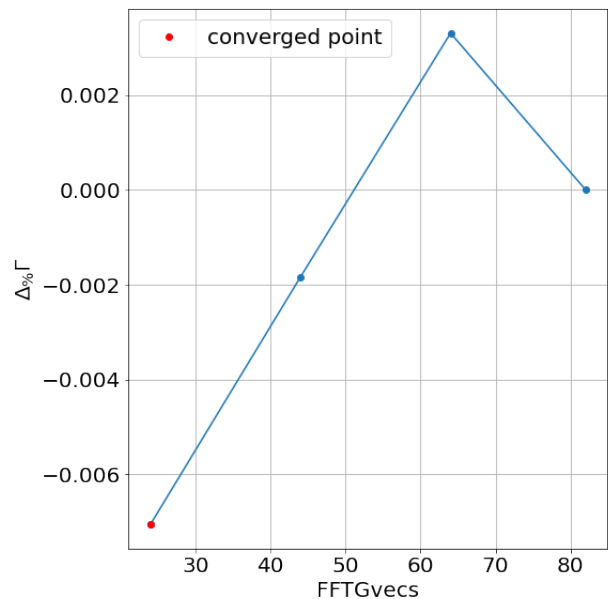
FIG. 7: \mathbf{k} -mesh convergence for silicon.FIG. 9: \mathbf{k} -mesh convergence for diamond.FIG. 8: Convergence of N_b and G_{cut} for diamond.

FIG. 10: FFT convergence for diamond.

can be left intact. This can speed up large-scale calculations where the file size of these matrices are large, since usually the disk read/write speed is the slowest during the calculations. Moreover, reusing the $U_{mn\mathbf{k}}$ means it will reach the same minimum as the Wannierization at DFT level, thus the Wannier interpolation accuracy of GW eigenenergies is expected to be similar to that at DFT level.

A. Effective band interpolation around given energy windows to reduce computational costs

The calculation of a large number of quasiparticle corrections can become easily computationally unfeasible for large systems. For example, in the case of PdCoO_2 ,[?] a bulk metallic system of interest for Fermi surface measurements, the minimum number of GW eigenvalues needed to obtain the interpolated band structure is $N_{QP} \sim 3 \cdot 10^4$. We propose here a method to effectively reduce the number of GW evaluation needed, if only a

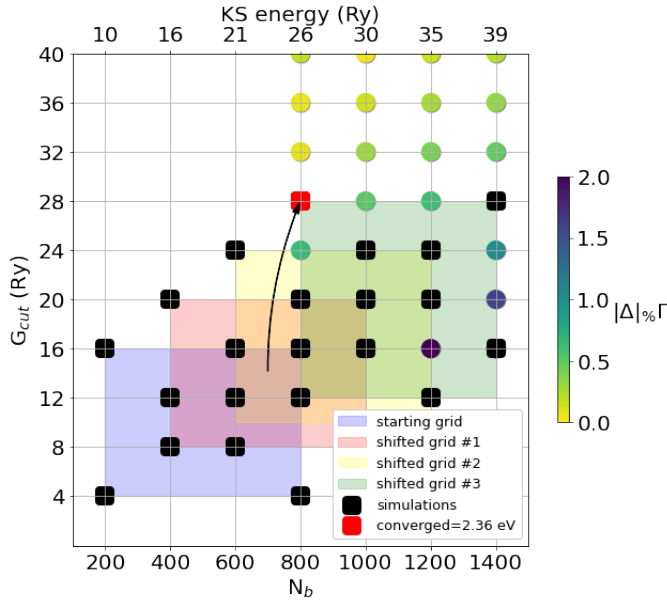


FIG. 11: Convergence of N_b and G_{cut} for ZnO.

given energy region of interest requires an accurate band interpolation. Within this approximation, the quasiparticle correction to KS eigenvalues is introduced in such a way to be the exact one in a given energy range, and replaced by a scissor and stretching evaluation outside. The exact GW correction goes continuously into the scis-

sored and stretched one, and viceversa, through a Fermi-Dirac smearing, considering an energy window centered at E_{center} and of width μ :

$$E_{GW}^{approx.} = \frac{E_{GW}^{true}}{1 + e^{\frac{|E_{KS} - E_{center}| - \mu}{T}}} + \left(1 - \frac{1}{1 + e^{\frac{|E_{KS} - E_{center}| - \mu}{T}}}\right) \times (A * E_{KS} + b) \quad (1)$$

The smearing parameter T is tuned in such a way to reduce the bump between the two different types of corrections. The E_{center} , in terms of KS energies, is user defined. In Fig. 13 are shown the results of the interpolation for different values of μ and T , considering $E_{center} = E_{Fermi}^{KS}$. We observe that results are in very good agreement ($\leq 10^{-2}$ eV) for $T \leq 10^{-2}$ eV. In particular for the metals case, we are often interested only in the region around the Fermi level, for example to compute the Fermi surface. This means that we require the exact GW correction to DFT only for a small region belonging to an energy window supposed to include the Fermi level, approximating the corrections for the other eigenvalues in such a way to still have a good Wannier interpolation but reducing the number of explicit GW eigenvalues. Anyway, we stress that since G_0W_0 is not particle conserving, a large region centered at the DFT Fermi energy is needed in order to possibly include the new and unknown GW Fermi level, that can be calculated a posteriori.

* corresponding author: miki.bonacci@nano.cnr.it

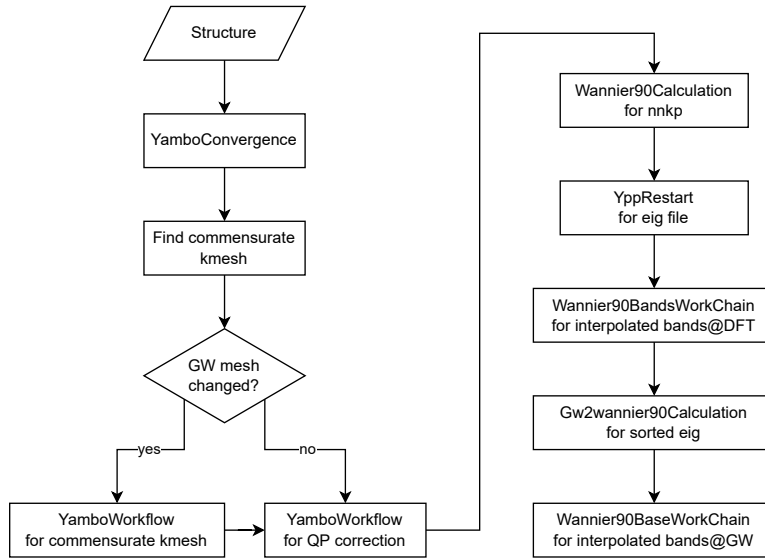


FIG. 12: Detailed flowchart of the `YamboWannier90WorkChain` for automated GW convergence and Wannier interpolated GW band structure. The workflow performs the `Yambo` convergence, searching of commensurate kpoint mesh between `Yambo` and `Wannier90`, and running the `Yambo` quasiparticle calculation. The QP correction is provided and the final steps of the flow comprise the Wannierizations and the band interpolations at DFT level and GW level.

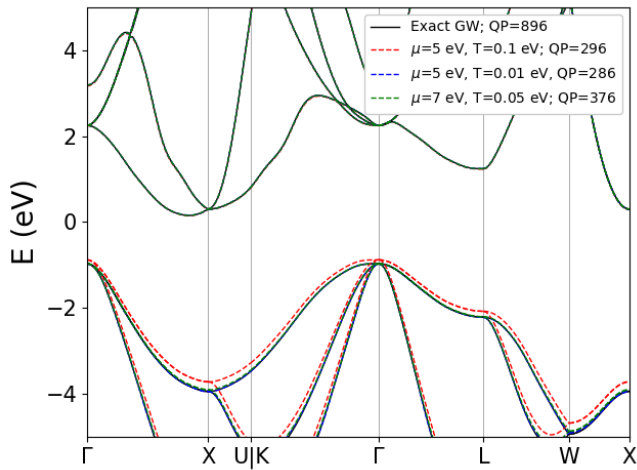


FIG. 13: **FD and scissor corrections for Silicon.** We observe a rather good agreement, around 10^{-2} eV, between the exact solution and the approximated ones for $T \leq 10^{-2}$ eV. E_{center} here is chosen to be the KS-DFT Fermi level.

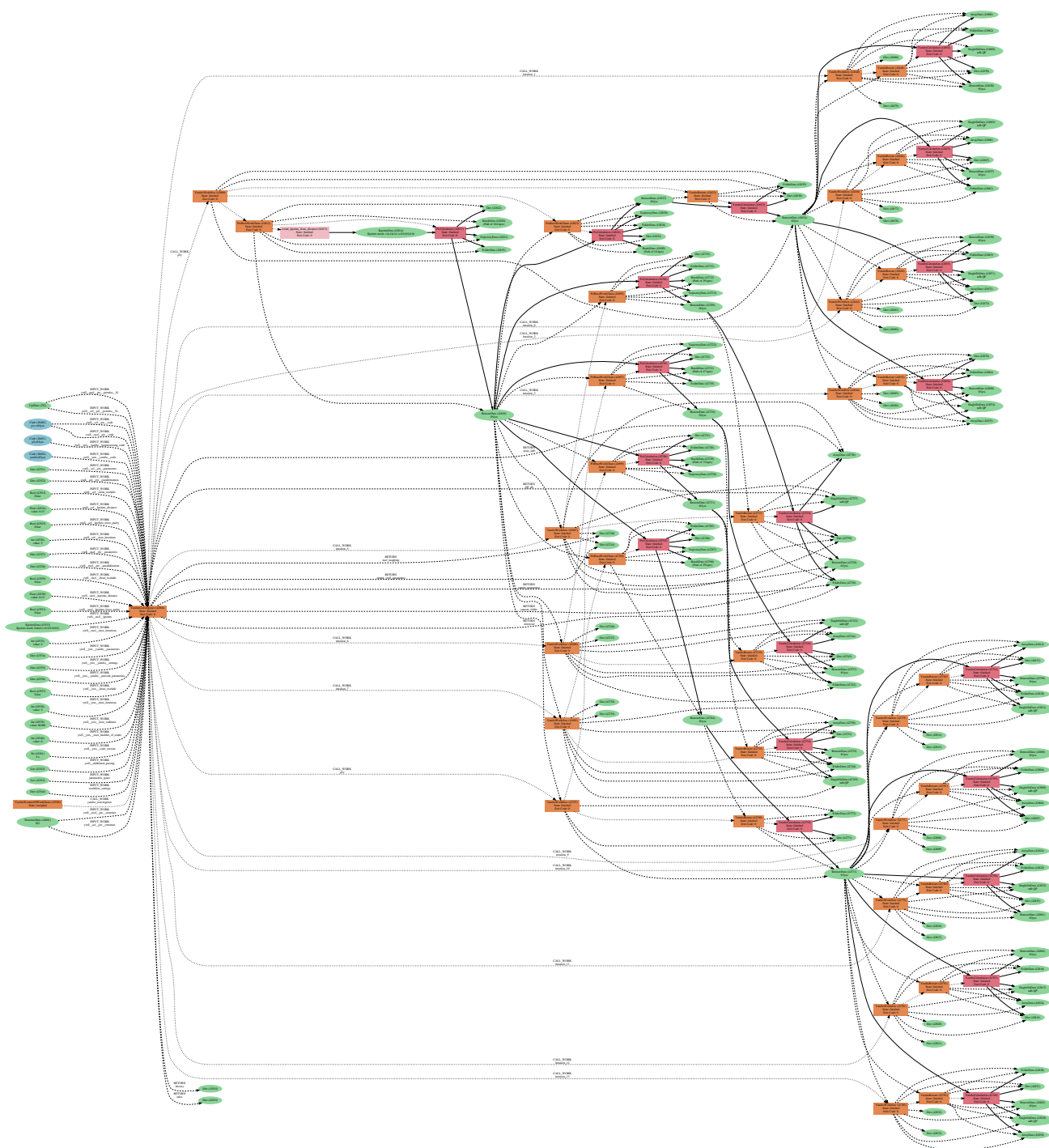


FIG. 14: **Example of provenance graph for YamboConvergence.** Provided the inputs (the first column of boxes from the left), the YamboConvergence calls a series of YamboWorkflows to perform the needed runs of PwCalculation and YamboCalculation, represented by the red boxes. Outputs are then generated and analysed by the workflow.